Electronic Research Archive

ERA, 34(9): 6249–6285.
DOI: 10.3934/era.2026274
Received: 07 May 2026
Revised: 16 June 2026
Accepted: 24 June 2026
Published: 16 July 2026

http://www.aimspress.com/journal/ERA

Research article

Coupled dynamic modeling and nonstationary vibration analysis of a double-cable hoist under rigid guide-roller contact excitation

Guoying Wang[1], Dongyue Li[2], Wanqiang Chen[1,*], Yongtao Wang[1,3] and Chengshuang Zhang[4]

[1] School of Machinery and Automation, Weifang University, Weifang 261061, China
[2] Department of Advanced Manufacturing and Robotics, College of Engineering, State Key Laboratory for Turbulence and Complex Systems, Peking University, Beijing 100871, China
[3] Shandong Key Laboratory of Intelligent Manufacturing Technology for Advanced Power Equipment, Weifang 261061, China
[4] Service Development Advancement Center of Science and Technology Shandong Province, Jinan 250101, China

* **Correspondence:** Email: wqchen@wfu.edu.cn.

Abstract: In this paper, a comprehensive coupled dynamic model was developed for a double-cable mine hoisting system to investigate nonstationary vibration responses induced by rigid-guide imperfections. The spatial motions of the cables in the longitudinal, transverse, and lateral directions were described by nonlinear partial differential equations (PDEs), whereas the cage dynamics and guide-roller interactions were formulated as coupled ordinary differential equations (ODEs). By incorporating time-varying cable lengths and rigid guide-roller contact excitation, the governing equations were transformed into a finite-dimensional ODE system using a normalized spatial coordinate and Galerkin projection. The numerical implementation was verified through modal, time-step, and no-guide-deviation benchmark analyses. Numerical simulations were then conducted to characterize the nonstationary dynamic behavior of the system under guide curvature and verticality deviations, with particular emphasis on tension inconsistency between the suspension strings. The model-based reference deviation amplitudes were further identified, providing a theoretical basis for assessing the influence of guide-structure geometric deviations on hoisting-operation safety.

Keywords: double-cable hoist; nonlinear partial differential equations; rigid guide; coupled dynamic model; tension inconsistency

1. Introduction

Flexible-cable hoisting systems are widely used in transportation applications, including deep-mine hoists [1–3], high-rise elevators [4,5], and telescopic cranes [6,7]. In ultra-deep mining, coupled double-cable hoists are essential for high-speed, heavy-load cage operation because they improve load distribution and provide safety redundancy. However, dynamic coupling between the cables can reduce operational reliability by increasing the system's sensitivity to external disturbances. In practice, manufacturing and assembly errors inevitably introduce curvature and verticality deviations along the rigid guides. During hoisting, these deviations act as end-boundary excitations and induce complex nonstationary cable vibrations. The resulting interaction between the two cables accelerates fatigue wear and may compromise operational safety. Therefore, accurate prediction and mitigation of nonstationary dynamic behavior induced by end-boundary excitation remain fundamental challenges in the design of flexible-cable hoisting systems.

Research on single-cable hoisting dynamics has established a substantial theoretical framework that can be broadly divided into two areas: Refined models for engineering systems such as elevators and deep-mine hoists, and fundamental theories for axially moving continua such as strings and beams. In engineering applications, dynamic models of high-rise elevator cables have evolved from simplified string or beam models with negligible bending stiffness [8] to more sophisticated nonlinear formulations that account for time-varying length [9], coupled vibration [10–12], bending stiffness [13], and boundary motion. Zhu et al. [8,13] developed nonlinear vibration models with small bending stiffness and moving boundaries to predict elevator-cable dynamics. Longitudinal, lateral, and coupled nonlinear responses of elevator cable-car systems have also been analyzed using refined spatial discretization and substructure methods [10,11]. Kaczmarczyk and Iwankiewicz [9] proposed deterministic equations of motion and stochastic models for high-speed cables in heavy-load structures, explicitly considering the effect of operating speed. Based on Hamilton's principle, Yang et al. [12] investigated nonlinear elevator vibrations and developed corresponding dynamic models. For ultra-deep mining applications, transient vibrations of hoisting cables under winding excitation have been examined. Models describing nonlinear modal interactions between catenary and suspension ropes have shown that harmful resonances can be mitigated by adjusting the operating velocity [14,15]. Collectively, these studies have clarified the internal coupling mechanisms of single-cable systems. From a theoretical perspective, the representation of cables as axially moving strings or beams has motivated extensive research. A range of analytical approaches has been adopted [16–19], including Hamilton's principle, the Kelvin viscoelastic model, the method of multiple scales, the differential quadrature element method, asymptotic expansion methods, and D'Alembert's principle. Numerical solutions are commonly obtained using the finite difference method [20] or the Galerkin method [21]. For complex vibration problems involving localized excitation, moving boundaries, and strong coupling, the accuracy of the spatial approximation is particularly important. In addition to classical finite-difference and Galerkin approaches, enriched approximation spaces have attracted attention in related discretization contexts [22–24]. These developments highlight the importance of accurate approximation strategies for complex coupled dynamic systems. These studies cover complex dynamic phenomena such as parametric resonance, internal resonance, high-mode-number resonance, and chaotic motion [25–28]. Research therefore spans linear and nonlinear dynamics, constant- and variable-length configurations, and simple and complex boundary conditions [29–32].

Despite these important contributions, most analyses remain limited to single linear continua or isolated cable systems. As a result, theoretical models cannot fully describe dynamic force redistribution and vibration coupling at the shared boundary of dual cables. They also provide limited insight into the mechanisms by which small boundary excitations generate interactive dynamic imbalance. A coupled dynamic model that captures inter-cable interaction is therefore required to understand and predict imbalance phenomena in double-cable hoisting systems. Several researchers have addressed the dynamics of multi-cable systems. Wang et al. [2] proposed a dynamic model for a coupled double-cable, double-drum winding hoist with flexible guides and clarified the complex coupling relationships in the system. Wang and Chen [33] developed a three-dimensional dynamic model for a double-cable winding hoisting system with flexible guides based on the substructure method and Lagrange's first-order equations. For four-cable-driven parallel suspension platforms with slack cables, a dynamic simulation model was developed to maintain platform stability through coordinated cable tensioning [1]. These studies demonstrate that the tension and motion states of individual cables are mutually constrained through a common end platform. However, a dynamic model for double-cable systems that explicitly incorporates contact interactions between the cage and rigid guides through the rollers remains lacking.

The dynamic response of cables subjected to boundary excitation has also received considerable attention. Researchers have focused mainly on the boundary conditions of axially moving continua and developed methods for treating complex boundary constraints. For example, the method of multiple scales [34], perturbation techniques [35], and the rapidly recursive extended method of characteristics [36] have been used to study the vibration of strings under external excitation. These researchers verified the effectiveness of such methods for analyzing string dynamics under boundary disturbances. Researchers have also examined the vibration responses of hoisting and elevator cable systems under various boundary excitations. Winding excitation [10,11], drive-system perturbations [37], and building sway [38] have been shown to induce significant vibration. The excitation frequencies may approach the natural frequencies of the system, thereby increasing the risk of resonance. Phenomena, such as the emergence of a newly ordered time scale under upper-end boundary excitation, have also been reported [39]. Three-time-scale perturbation methods and interior-layer analyses have been applied to investigate these dynamics and have been verified through numerical simulations [38,40,41]. These findings identify boundary excitation as a key source of complex vibration and resonance in cable systems. Nevertheless, most studies represent boundary excitation as a prescribed displacement at the cable end, rather than modeling the physical contact mechanism that generates the excitation.

To the best of our knowledge, analyses of double-cable hoist dynamics are largely based on flexible-guide and simplified boundary excitation models. A dynamic model that accurately captures the nonlinear contact mechanics at the rigid guide-roller interfaces has not been established. In addition, the excitation mechanisms associated with different types of guide deviation have not been investigated, and quantitative safety limits for these deviations remain unavailable.

In this paper, we develop a longitudinal-transverse-lateral coupled dynamic model for a double-cable hoist that accounts for the interactions among the rigid guides, guide rollers, and cage. The model is then used to systematically examine how two types of nonlinear contact boundary excitation affect the nonstationary dynamics of the system, with particular attention to inter-cable tension inconsistency. The results provide a theoretical basis for the safe operation of double-cable hoisting systems. The major contributions of this study are summarized as follows:

1). A longitudinal-transverse-lateral coupled dynamic model is developed for a double-cable hoist for the first time. The model couples the nonlinear PDEs governing the spatial motions of the cables with the ODEs describing rigid guide-roller contact excitation and time-varying cable lengths.

2). The nonstationary dynamic responses of the hoisting system are systematically characterized under two representative rigid-guide imperfections, namely curvature and verticality deviations.

3). Quantitative reference amplitudes for curvature and verticality deviations are identified for the studied hoisting system based on the adopted tension-inconsistency criterion. In addition, numerical verification and parameter-sensitivity analyses are conducted to evaluate the reliability and system dependence of the predicted responses.

The remainder of this paper is organized as follows: In Section 2, the end-boundary excitations are described, and the physical model of the hoisting system is presented. In Section 3, the coupled equations of motion for the double-cable hoist are derived based on Hamilton's principle. In Section 4, the equations of motion are spatially discretized via the Galerkin method. In Section 5, numerical simulations for the dynamic model are conducted, and the nonstationary vibration responses of the system are analyzed. In Section 6, the major conclusions of this paper are summarized.

2. Model description

To facilitate the presentation of the coupled dynamic model, the key variables and their physical interpretations used throughout this study are summarized in Table 1.

Table 1. Definitions and physical interpretations of key variables.

Variable Symbol	Physical Interpretation
$u_{ck}(x,t)$, $w_{ck}(x,t)$, $v_{ck}(x,t)$	Vibration displacements of the k-th inclined string in the longitudinal, transverse, and lateral directions, respectively.
$u_{pk}(x,t)$, $w_{pk}(x,t)$, $v_{pk}(x,t)$	Vibration displacements of the k-th suspension string in the longitudinal, transverse, and lateral directions, respectively.
l_{ck}	Length of the k-th inclined string.
$l_{pk}(t)$	Length of the k-th suspension string.
$T_{ck}(x,t)$	Static tension in the k-th inclined string.
$T_{pk}(x,t)$	Static tension in the k-th suspension string.
$\varepsilon_{ck}(x,t)$	Elastic strain of the k-th inclined string.
$\varepsilon_{pk}(x,t)$	Elastic strain of the k-th suspension string.
s_k	Horizontal distance between the k-th suspension string and the top center of the cage.
h	Vertical distance from the cage center of mass to its top edge.
$e_{c,\max}$	Maximum curvature deviation of the rigid-guide section.
$e_{p,\max}$	Maximum verticality deviation of the rigid-guide section.
l_g	Length of a single rigid-guide section.
$V(t)$	Operating velocity of the hoist.
N_e	Total number of rigid-guide sections.
y_r, x_r	Vibration displacements of the cage center of mass in the longitudinal and transverse directions, respectively.
$\theta(t)$	Rotational angle of the cage.

Continued on next page

Variable Symbol	Physical Interpretation
y_{gk}, x_{gk}	Vibration displacements at the end of the k-th suspension string in the longitudinal and transverse directions, respectively.
V_{yr}, V_{xr}	Vibration velocities of the cage center of mass in the longitudinal and transverse directions, respectively.
d_e	Static clearance between the cage and each rigid guide.
ρ	Cable mass per unit length
I_d	Moment of inertia of the drum.
I_h	Moment of inertia of the guide pulley.
$a(t)$	Operating acceleration of the system.
m	Mass of the cage.
m_k	Hoisted load mass associated with the k-th cable.
I_p	Moment of inertia of the cage.
c_h	Friction coefficient between the cable and the guide pulley.
β_h	Wrap angle of the cable around the guide pulley.
g	Gravitational acceleration.
R_d	Radius of the drum.
R_h	Radius of the guide pulley.
μ_e	Friction coefficient between the rigid guide and the roller.
α	Angle between the inclined string and the horizontal axis.
$S_k(t)$	Dynamic clearance between the k-th rigid guide and the cage.
d	Nominal clearance between the roller and the rigid guide.
k_r	Roller stiffness.
k_g	Rigid-guide stiffness.
k_p	Equivalent contact stiffness between the rigid guide and the roller.
l_x	Vertical distance between the roller and the upper end of the rigid-guide section.
EI	Bending rigidity of the rigid guide.
EA	Tensile stiffness of the cable.
c_d	Damping coefficient of the roller.
a_{yr}, a_{xr}	Vibration accelerations of the cage center of mass in the longitudinal and transverse directions, respectively.

2.1. End-boundary excitations

In practical hoisting systems, curvature and verticality deviations are inevitably introduced along the rigid guides by manufacturing and assembly tolerances. These geometric imperfections are transmitted to the cage through the guide rollers and subsequently induce cage rotation. Through this roller-based transmission mechanism, deviations in the rigid guides are converted into dynamic boundary excitations, which trigger coupled longitudinal, transverse, and lateral vibrations of the two cables. As a result, inconsistencies in vibration displacement and inter-cable tension may occur. Figure 1 illustrates the curvature and verticality deviations of the rigid guide, where the red and blue lines denote the curvature and verticality profiles, respectively.

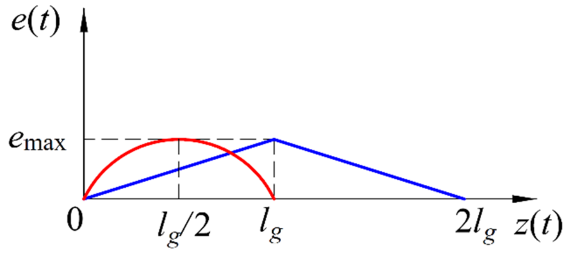

Figure 1. Schematic of the spatial curvature and verticality deviation profiles of the rigid guide.

In this paper, the two types of guide deviation are represented by spatial functions. Since the cage moves along the rigid guides, the spatial guide deviations are converted into time-dependent end-boundary excitations through the traveled distance of the cage.

The curvature deviation of a rigid guides section originates from warping during manufacturing. It is described by a half-sine spatial profile in each guide section as follows:

$$e_c(t)=e_c(z(t))=e_{c,\max}\sin\left(\frac{\pi\left(z(t)-(j-1)l_g\right)}{l_g}\right),\quad (j-1)l_g\le z(t)\le jl_g,\quad j=1,2,\ldots,N_e, \tag{2.1}$$

where j is the section index, and $z(t)$ is the traveled distance of the cage along the rigid guide $z(t)=\int_0^t V(\tau)d\tau$.

Verticality deviations along the rigid guides are mainly caused by assembly tolerances and appear as relative inclinations between adjacent guide sections at their structural joints. Accordingly, the verticality deviation is described by a triangular profile as follows:

$$e_p(t)=e_p(z(t))=\begin{cases} e_{p,\max}\dfrac{z(t)-(j-1)l_g}{l_g}, & (j-1)l_g\le z(t)\le jl_g,\ j=1,3,5,\ldots,N_e \\ e_{p,\max}\left(1-\dfrac{z(t)-(j-1)l_g}{l_g}\right), & (j-1)l_g\le z(t)\le jl_g,\ j=2,4,6,\ldots,N_e \end{cases}. \tag{2.2}$$

Equations (2.1) and (2.2) indicate that the guide deviations are spatial properties of the rigid guide, whereas the corresponding end-boundary excitations become time-dependent because the cage moves along the guide.

2.2. Dynamic model description

The dynamic model of the coupled double-cable hoist is shown in Figure 2. The hoisting system consists of two drums, two flexible cables, two guide pulleys, a cage, two rigid guides, and associated guide rollers. Each cable includes an inclined string and a suspension string, which are coupled at the corresponding guide pulley. The two cables are further dynamically coupled through the common cage. In the transverse plane of the hoist, two types of geometric deviation act as end-boundary excitations. As shown in Figure 2, the black lines represent the nominal operating configuration, whereas the red lines indicate the perturbed configuration under end excitation. These deviations cause nonlinear contact between the rollers and rigid guides, disturb the cage kinematics, and dynamically modify the boundary conditions of the two cables, thereby exciting coupled vibration. To capture these interactions, the roller-guide interfaces are modeled as equivalent spring-damper systems that include structural clearance and contact stiffness.

To establish the equations of motion, the midpoints of the two cables at the contact regions with the winding drums and guide pulleys are used as the origins of the reference coordinate systems $O_cX_cY_c$ and $O_pX_pY_p$. The key position coordinates are defined as follows: l_{cbk} and l_{cek} denote the coordinates of the tangent points where the k-th inclined string contacts the drum and guide pulley, respectively. Similarly, l_{pbk} denotes the tangent point of the k-th suspension string at the guide pulley, and l_{pek} denotes its terminal connection point at the cage.

The dynamic model of the coupled double-cable hoisting system is derived under the following assumptions:

1). The two cables are made of homogeneous continuous materials.

2). The cable mass per unit length, cable tensile stiffness, and rigid-guide bending stiffness are constant.

3). The nonlinear vibration displacements of the cables are much smaller than their total lengths.

4). Each rigid-guide section contains a geometric deviation.

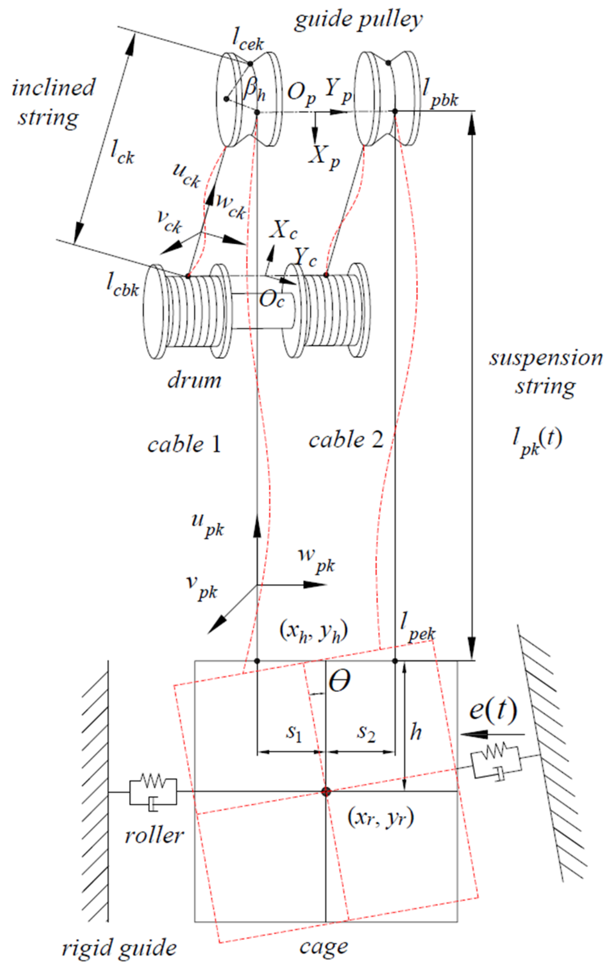

Figure 2. Schematic of the proposed coupled double-cable hoisting-system model.

Regarding the notation used in this paper, subscripts c and p denote the inclined and suspension strings, respectively, and $k \in \{1,2\}$ identifies the cable. Partial derivatives with respect to time t and the spatial coordinate x are denoted by an overdot and a prime, respectively. For brevity, when no ambiguity arises, explicit spatiotemporal dependencies are omitted; thus, $u(x,t)$, $w(x,t)$, $v(x,t)$, $x(t)$, $T(x,t)$, $\varepsilon(x,t)$, $l_p(t)$, $e(t)$, $V(t)$, $\theta(t)$, $S(t)$, and $a(t)$ are written as u, w, v, x, T, ε, l_p, e, V, θ, S, and a, respectively. The matrix and vector functions **L**, **x**, **u**, **w**, **v**, **i**, **j**, and **k** are defined as follows:

$$\mathbf{L}=\begin{bmatrix}\mathbf{L}_{c1} & \mathbf{L}_{c2} & \mathbf{L}_{p1} & \mathbf{L}_{p2}\end{bmatrix}^{\mathrm{T}},\ \mathbf{x}=\begin{bmatrix}\mathbf{x}_c & \mathbf{x}_p\end{bmatrix}^{\mathrm{T}},\ \mathbf{x}_c=\begin{bmatrix}x_{c1} & x_{c2}\end{bmatrix}^{\mathrm{T}},\ \mathbf{x}_p=\begin{bmatrix}x_{p1} & x_{p2}\end{bmatrix}^{\mathrm{T}},$$

$$\mathbf{u}=\begin{bmatrix}\mathbf{u}_c & \mathbf{u}_p\end{bmatrix}^{\mathrm{T}},\ \mathbf{u}_c=\begin{bmatrix}u_{c1} & u_{c2}\end{bmatrix}^{\mathrm{T}},\ \mathbf{u}_p=\begin{bmatrix}u_{p1} & u_{p2}\end{bmatrix}^{\mathrm{T}},\ \mathbf{w}=\begin{bmatrix}\mathbf{w}_c & \mathbf{w}_p\end{bmatrix}^{\mathrm{T}},$$

$$\mathbf{w}_c=\begin{bmatrix}w_{c1} & w_{c2}\end{bmatrix}^{\mathrm{T}},\ \mathbf{w}_p=\begin{bmatrix}w_{p1} & w_{p2}\end{bmatrix}^{\mathrm{T}},\ \mathbf{v}=\begin{bmatrix}\mathbf{v}_c & \mathbf{v}_p\end{bmatrix}^{\mathrm{T}},\ \mathbf{v}_c=\begin{bmatrix}v_{c1} & v_{c2}\end{bmatrix}^{\mathrm{T}},$$

$$\mathbf{v}_p=\begin{bmatrix}v_{p1} & v_{p2}\end{bmatrix}^{\mathrm{T}},\ \mathbf{i}=\mathrm{diag}\begin{bmatrix}\mathbf{i}_c & \mathbf{i}_p\end{bmatrix},\ \mathbf{i}_c=\mathrm{diag}\begin{bmatrix}\mathbf{i}_{c1} & \mathbf{i}_{c2}\end{bmatrix},\ \mathbf{i}_p=\mathrm{diag}\begin{bmatrix}\mathbf{i}_{p1} & \mathbf{i}_{p2}\end{bmatrix},$$

$$\mathbf{j}=\mathrm{diag}\begin{bmatrix}\mathbf{j}_c & \mathbf{j}_p\end{bmatrix},\ \mathbf{j}_c=\mathrm{diag}\begin{bmatrix}\mathbf{j}_{c1} & \mathbf{j}_{c2}\end{bmatrix},\ \mathbf{j}_p=\mathrm{diag}\begin{bmatrix}\mathbf{j}_{p1} & \mathbf{j}_{p2}\end{bmatrix},$$

$$\mathbf{k}=\mathrm{diag}\begin{bmatrix}\mathbf{k}_c & \mathbf{k}_p\end{bmatrix},\ \mathbf{k}_c=\mathrm{diag}\begin{bmatrix}\mathbf{k}_{c1} & \mathbf{k}_{c2}\end{bmatrix},\ \mathbf{k}_p=\mathrm{diag}\begin{bmatrix}\mathbf{k}_{p1} & \mathbf{k}_{p2}\end{bmatrix}.$$

3. Governing equations of motion

According to finite-deformation theory for continuous media, the displacement matrix of an arbitrary moving reference point along the hoisting cable is written as follows:

$$\mathbf{L}=\left(\mathbf{x}+\mathbf{u}\right)\mathbf{i}+\mathbf{w}\mathbf{j}+\mathbf{v}\mathbf{k}, \tag{3.1}$$

where **i**, **j**, and **k** are the orthonormal basis vectors along the X-, Y-, and Z-axes, respectively.

The velocity matrix of the moving reference point on the cable is expressed as

$$\mathbf{V}=\left(\dot{\mathbf{x}}+\frac{\mathrm{D}\mathbf{u}}{\mathrm{D}t}\right)\mathbf{i}+\frac{\mathrm{D}\mathbf{w}}{\mathrm{D}t}\mathbf{j}+\frac{\mathrm{D}\mathbf{v}}{\mathrm{D}t}\mathbf{k}, \tag{3.2}$$

where $\mathbf{V}=\begin{bmatrix}\mathbf{V}_{c1} & \mathbf{V}_{c2} & \mathbf{V}_{p1} & \mathbf{V}_{p2}\end{bmatrix}^{\mathrm{T}}$ and $\dfrac{\mathrm{D}(\bullet)}{\mathrm{D}t}=\dfrac{\partial(\bullet)}{\partial t}+V\dfrac{\partial(\bullet)}{\partial x}$.

The displacement and velocity vectors at the winding drums are expressed as

$$\begin{cases}\mathbf{L}_d=\left(\mathbf{l}_c+\mathbf{u}\left(l_{cb},t\right)\right)\mathbf{i}_c+\mathbf{w}\left(l_{cb},t\right)\mathbf{j}_c+\mathbf{v}\left(l_{cb},t\right)\mathbf{k}_c\\ \mathbf{V}_d=\left(V+\dfrac{\mathrm{D}\mathbf{u}\left(l_{cb},t\right)}{\mathrm{D}t}\right)\mathbf{i}_c+\dfrac{\mathrm{D}\mathbf{w}\left(l_{cb},t\right)}{\mathrm{D}t}\mathbf{j}_c+\dfrac{\mathrm{D}\mathbf{v}\left(l_{cb},t\right)}{\mathrm{D}t}\mathbf{k}_c\end{cases}, \tag{3.3}$$

where $\mathbf{L}_d = [\mathbf{L}_{d1} \quad \mathbf{L}_{d2}]^{\mathrm{T}}$, $\mathbf{V}_d = [\mathbf{V}_{d1} \quad \mathbf{V}_{d2}]^{\mathrm{T}}$, and $\mathbf{l}_c = [l_{c1} \quad l_{c2}]^{\mathrm{T}}$.

Similarly, the displacement and velocity vectors at the guide pulleys are expressed as

$$\begin{cases} \mathbf{L}_h = \left(\mathbf{l}_c + \mathbf{u}(l_{ce},t)\right)\mathbf{i}_c + \mathbf{w}(l_{ce},t)\,\mathbf{j}_c + \mathbf{v}(l_{ce},t)\mathbf{k}_c \\ \mathbf{V}_h = \left(V + \dfrac{\mathrm{D}\mathbf{u}(l_{ce},t)}{\mathrm{D}t}\right)\mathbf{i}_c + \dfrac{\mathrm{D}\mathbf{w}(l_{ce},t)}{\mathrm{D}t}\mathbf{j}_c + \dfrac{\mathrm{D}\mathbf{v}(l_{ce},t)}{\mathrm{D}t}\mathbf{k}_c \end{cases}, \tag{3.4}$$

where $\mathbf{L}_h = [\mathbf{L}_{h1} \quad \mathbf{L}_{h2}]^{\mathrm{T}}$ and $\mathbf{V}_h = [\mathbf{V}_{h1} \quad \mathbf{V}_{h2}]^{\mathrm{T}}$.

In this study, we focus on the dynamic effects of end-boundary excitations localized in the transverse plane of the rigid guides, where two types of disturbance-induced deviation are considered. For modeling purposes, lateral rotation of the cage is neglected. The displacement vector of the cage is expressed as follows:

$$\mathbf{L}_r = x_r\mathbf{i}_r + y_r\mathbf{j}_r. \tag{3.5}$$

The kinematic relationships governing the longitudinal and transverse displacements between the ends of the suspension strings and the cage are expressed as follows:

$$\begin{cases} \mathbf{x}_g = \mathbf{l}_p + \mathbf{u}_p\left(l_{pe}(t),t\right) \\ \mathbf{y}_g = \mathbf{s} + \mathbf{w}_p\left(l_{pe}(t),t\right) \end{cases}, \tag{3.6}$$

where $\mathbf{x}_g = [x_{g1} \quad x_{g2}]^{\mathrm{T}}$, $\mathbf{l}_p = [l_{p1} \quad l_{p2}]^{\mathrm{T}}$, $\mathbf{s} = [-s_1 \quad s_2]^{\mathrm{T}}$, and $\mathbf{y}_g = [y_{g1} \quad y_{g2}]^{\mathrm{T}}$.

Because the cage rotation angle is sufficiently small, the small-angle approximations $\sin\theta \approx \theta$ and $\tan\theta \approx \theta$ are valid and are applied below. With reference to Figure 2, the geometric compatibility between the translational displacements of the cage center of mass and the terminal displacements of the suspension strings is given by

$$\begin{cases} x_{g1} = x_h - s_1\cos\theta - h\dfrac{\theta}{2}\cos\theta \\ x_{g2} = x_h + s_2\cos\theta - h\dfrac{\theta}{2}\cos\theta \\ y_{g1} = y_h + s_1\theta + h\dfrac{\theta^2}{2} \\ y_{g2} = y_h - s_2\theta + h\dfrac{\theta^2}{2} \end{cases}, \tag{3.7}$$

where

$$\begin{cases} x_h = x_r - h \\ y_h = y_r - h\dfrac{\theta}{2} \end{cases}$$

Combining Eqs (3.6) and (3.7), the longitudinal and transverse vibration displacements of the cage center of mass are obtained as follows:

$$\begin{cases} x_r = \dfrac{1}{2}\sum_{k=1}^{2}\left(l_{pk} + u\left(l_{pek},t\right)\right) + h\left(1 - \dfrac{\theta^2}{2}\right) + \dfrac{\left(s_2 - s_1\right)\theta}{2} \\ y_r = \dfrac{1}{2}\sum_{k=1}^{2} w\left(l_{pek},t\right) + h\dfrac{\theta}{2}\left(1+\cos\theta\right) - \dfrac{\left(s_2 - s_1\right)\cos\theta}{2} \end{cases}. \tag{3.8}$$

The velocity vector of the cage is written as follows:

$$\mathbf{V}_r = V_{xr}\mathbf{i}_r + V_{yr}\mathbf{j}_r. \tag{3.9}$$

The longitudinal and transverse velocities of the cage center of mass are expressed as

$$\begin{cases} V_{xr} = \dfrac{1}{2}\sum_{k=1}^{2}\left(V_{pk} + V_{pk}u'\left(l_{pek},t\right) + \dot{u}\left(l_{pek},t\right)\right) - \dfrac{1}{2}h\theta\dot{\theta}\left(\left(1+\dfrac{\theta^2}{4}\right) + \cos\theta\right) + \dfrac{\left(s_2 - s_1\right)\cos\theta\dot{\theta}}{2} \\ V_{yr} = \dfrac{1}{2}\sum_{k=1}^{2}\left(V_{pk}w'\left(l_{pek},t\right) + \dot{w}\left(l_{pek},t\right)\right) + \dfrac{h\dot{\theta}}{2}\left(\left(1+\cos\theta\right)\left(1+\dfrac{\theta^2}{4}\right) - \dfrac{\theta^2}{2}\right) - \dfrac{\left(s_2 - s_1\right)\theta\dot{\theta}}{2} \end{cases}, \tag{3.10}$$

where

$$\begin{cases} \sin\theta = \dfrac{l_{p1} - l_{p2} + u\left(l_{pe1},t\right) - u\left(l_{pe2},t\right)}{s_1 + s_2}, & \left|\sin\theta\right| < \dfrac{d_e + e}{l_g} \\ \sin\theta = \dfrac{d_e + e}{l_g}, & \left|\sin\theta\right| \ge \dfrac{d_e + e}{l_g} \end{cases}.$$

The total kinetic energy of the double-cable hoisting system is written as follows:

$$\begin{aligned} E_k = {} & \frac{1}{2}\rho\sum_{k=1}^{2}\int_{l_{cbk}}^{l_{cek}} \mathbf{V}_{ck}\cdot\mathbf{V}_{ck}\,\mathrm{d}x + \frac{1}{2}\rho\sum_{k=1}^{2}\int_{l_{pbk}}^{l_{pek}} \mathbf{V}_{pk}\cdot\mathbf{V}_{pk}\,\mathrm{d}x \\ & + \frac{1}{2}\sum_{k=1}^{2}\frac{I_d}{R_d^2}\mathbf{V}_{dk}\cdot\mathbf{V}_{dk} + \frac{1}{2}\sum_{k=1}^{2}\frac{I_h}{R_h^2}\mathbf{V}_{hk}\cdot\mathbf{V}_{hk} + \frac{1}{2}m\mathbf{V}_r\cdot\mathbf{V}_r + \frac{1}{2}I_p\dot{\theta}^2 \end{aligned}. \tag{3.11}$$

The static tension at the moving reference point along the cable is given by

$$\mathbf{T} = \mathbf{m}g + \rho g\mathbf{l} + \mu_e k_p\mathbf{S}, \tag{3.12}$$

where $\mathbf{T}=\begin{bmatrix}\mathbf{T}_c & \mathbf{T}_p\end{bmatrix}^{\mathrm{T}}$, $\mathbf{T}_c=\begin{bmatrix}T_{c1} & T_{c2}\end{bmatrix}^{\mathrm{T}}$, $\mathbf{T}_p=\begin{bmatrix}T_{p1} & T_{p2}\end{bmatrix}^{\mathrm{T}}$, $\mathbf{m}=\begin{bmatrix}m_1 & m_2 & m_1 & m_2\end{bmatrix}^{\mathrm{T}}$, and $\mathbf{S}=\begin{bmatrix}0 & 0 & S_1 & S_2\end{bmatrix}^{\mathrm{T}}$.

Furthermore, the distance vector $\mathbf{l}$ is given by

$$\mathbf{l}=\begin{bmatrix}1 & 0\\ 0 & 1\end{bmatrix}\begin{bmatrix}\mathbf{l}_P\\ \mathbf{l}_P\end{bmatrix}-\begin{bmatrix}\sin\alpha & 0\\ 0 & 0\end{bmatrix}\begin{bmatrix}\mathbf{l}_c\\ \mathbf{l}_c\end{bmatrix}+\begin{bmatrix}\sin\alpha & 0\\ 0 & -1\end{bmatrix}\begin{bmatrix}\mathbf{x}_c\\ \mathbf{x}_P\end{bmatrix}, \tag{3.13}$$

where

$$\begin{bmatrix}m_1\\ m_2\end{bmatrix}=m\begin{bmatrix}-\left(\left(s_1+s_2\right)\cos\theta\right)^{-1}\\ \left(\left(s_1+s_2\right)\cos\theta\right)^{-1}\end{bmatrix}\begin{bmatrix}x_{g1} & 0\\ 0 & x_{g2}\end{bmatrix},$$

$$k_p=\begin{cases}k_r, & l_x=0\\ \dfrac{k_r k_g}{k_r+k_g}, & 0<l_x<l_g\\ k_r, & l_x=l_g\end{cases}, \text{ and } k_g=\frac{3l_g EI}{\left(l_g-l_x\right)^2 l_x^2},\ \ l_x\in\left(0,\ l_g\right).$$

The cable excitation is induced by geometric deviations of the rigid guides, which are transmitted through the guide rollers. The rigid guide-roller assembly is modeled as a contact-mechanics subsystem with a clearance gap and equivalent stiffness and is integrated into the overall system. The dynamic clearance between the rigid-guide sections and the cage is expressed as follows:

$$\begin{cases}\mathbf{S}_p=\left[S_1, S_2\right]^T,\\ S_k=\begin{cases}hf_k+e_k-d, & \text{if } hf_k+e_k-d>0,\\ 0, & \text{if } hf_k+e_k-d\le 0,\end{cases} k=1,2\end{cases}, \tag{3.14}$$

where $\mathbf{f}=\begin{bmatrix}\theta & -\theta\end{bmatrix}^{\mathrm{T}}$ and $\mathbf{e}=\begin{bmatrix}e_1 & e_2\end{bmatrix}^{\mathrm{T}}$.

Here, f_k and e_k are the k-th components of $\mathbf{f}$ and $\mathbf{e}$, respectively. Therefore, the unilateral contact condition is applied componentwise, and the contact state of each guide–roller pair is judged independently. Contact occurs only when the local relative displacement $hf_k + e_k$ exceeds the nominal clearance d. In the baseline simulations, the deviation is applied to one guide while the opposite guide is assumed to remain nominal; namely, $e_1 = e_c(z(t))$ or $e_p(z(t))$, and $e_2 = 0$. The formulation can also represent the case in which both guides have independent deviations by assigning nonzero values to e_1 and e_2.

Accordingly, the elastic potential energy of the overall system is expressed as follows:

$$E_p=\sum_{k=1}^{2}\int_{l_{cbk}}^{l_{cek}} T_{ck}\varepsilon_{ck}\mathrm{d}x+\frac{1}{2}\sum_{k=1}^{2}\int_{l_{cbk}}^{l_{cek}} EA\varepsilon_{ck}^2\mathrm{d}x+\sum_{k=1}^{2}\int_{l_{pbk}}^{l_{pek}} T_{pk}\varepsilon_{pk}\mathrm{d}x+\frac{1}{2}\sum_{k=1}^{2}\int_{l_{pbk}}^{l_{pek}} EA\varepsilon_{pk}^2\mathrm{d}x+\frac{1}{2}\sum_{k=1}^{2}k_p S_k^2. \tag{3.15}$$

According to the von Kármán strain theory, the strain-displacement relationship for the cable is written as follows:

$$\boldsymbol{\varepsilon} = \mathbf{u}' + \frac{1}{2}\bar{\mathbf{w}}' \cdot \mathbf{w}' + \frac{1}{2}\bar{\mathbf{v}}' \cdot \mathbf{v}', \tag{3.16}$$

where $\boldsymbol{\varepsilon} = \begin{bmatrix} \boldsymbol{\varepsilon}_c & \boldsymbol{\varepsilon}_p \end{bmatrix}^{\mathrm{T}}$, $\boldsymbol{\varepsilon}_c = \begin{bmatrix} \varepsilon_{c1} & \varepsilon_{c2} \end{bmatrix}^{\mathrm{T}}$, $\boldsymbol{\varepsilon}_p = \begin{bmatrix} \varepsilon_{p1} & \varepsilon_{p2} \end{bmatrix}^{\mathrm{T}}$, $\bar{\mathbf{w}} = \mathrm{diag}\begin{bmatrix} w_{c1} & w_{c2} & w_{p1} & w_{p2} \end{bmatrix}$, and $\bar{\mathbf{v}} = \mathrm{diag}\begin{bmatrix} v_{c1} & v_{c2} & v_{p1} & v_{p2} \end{bmatrix}$.

The von Kármán strain-displacement relationship accounts for the geometrically nonlinear coupling among the longitudinal, transverse, and lateral vibration modes. Accordingly, the gravitational potential energy of the double-cable hoisting system is written as follows:

$$E_g = -\sum_{k=1}^{2} \int_{l_{pbk}}^{l_{pek}} \rho g u_{pk} \mathrm{d}x + \sum_{k=1}^{2} \int_{l_{cbk}}^{l_{cek}} \rho g \sin\alpha u_{ck} \mathrm{d}x - \sum_{k=1}^{2} \rho g l_{pk} + \sum_{k=1}^{2} \rho g l_{ck} \sin\alpha - m g y_r. \tag{3.17}$$

In practical hoisting systems, due to factors such as preload, clearance, impact, wear, local deformation, and possible intermittent contact, the interaction between the guide rollers and the rigid guides becomes highly complex. This model does not aim to provide a detailed description of the local contact physical mechanisms. Instead, it is primarily intended to capture the dominant global dynamic characteristics of the coupled cable-cage system and to describe the general trends induced by parameter variations. Therefore, a spring-damper model with clearance is adopted to represent the interaction between the guide rollers and the rigid guides. This approach provides a simple and efficient way to model the primary unilateral contact mechanism. The spring-damper model is expressed as follows:

$$f_{gk} = k_p S_k + c_d \dot{S}_k. \tag{3.18}$$

The total virtual work of the double-cable hoisting system is given by:

$$\delta W = -\sum_{k=1}^{2} c_h \left(V + \dot{u}_{ck}\left(l_{ce}, t\right) \right) \delta u_{ck}\left(l_{ce}, t\right) + \sum_{k=1}^{2} f_{gk} \delta w_{pk}\left(l_{pe}, t\right). \tag{3.19}$$

Using Hamilton's principle, the governing equations of motion for the coupled double-cable hoisting system are written as follows:

$$\int_{t_1}^{t_2} \left(\delta E_k - \delta E_p - \delta E_g + \delta W \right) \mathrm{d}t = 0. \tag{3.20}$$

The system satisfies homogeneous Dirichlet boundary conditions at $x_c = 0$ and $x_p = 0$, where all translational displacements and corresponding velocities are zero. At the guide pulley, transverse and lateral vibrations of the inclined and suspension strings are suppressed by the pulley grooves; therefore, the displacements in these directions are neglected. In the longitudinal direction, the cables are modeled as slipping axially relative to the pulley interface. The resulting elastic tension-continuity condition [42] for the cable segments is expressed as follows:

$$EA\mathbf{u}_c'\left(l_{ce},t\right)=e^{c_h\beta_h}EA\mathbf{u}_p'\left(l_{pb},t\right). \tag{3.21}$$

At the initial state ($t = 0$), the relationship between the elastic and static tensions in the strings and the corresponding longitudinal displacement profile are given by

$$\mathbf{T}\left(x,0\right)=EA\begin{bmatrix}\left(\mathbf{u}_c'\left(x,0\right)\right)^{\mathrm{T}}\\ \left(\mathbf{u}_p'\left(x,0\right)\right)^{\mathrm{T}}-\left(\mathbf{u}_c'\left(l_{ce},0\right)\right)^{\mathrm{T}}\end{bmatrix}, \tag{3.22}$$

$$\begin{bmatrix}\mathbf{u}_c\left(x,0\right)\\ \mathbf{u}_p\left(x,0\right)\end{bmatrix}=\begin{bmatrix}\dfrac{\overline{\mathbf{T}}_c\left(x,0\right)}{EA} & 0\\ 0 & \dfrac{\overline{\mathbf{T}}_p\left(x,0\right)+\overline{\mathbf{T}}_c\left(l_{ce},0\right)}{EA}\end{bmatrix}\begin{bmatrix}\mathbf{x}_c\\ \mathbf{x}_p\end{bmatrix}, \tag{3.23}$$

where $\overline{\mathbf{T}}_c\left(x,0\right)=\mathrm{diag}\left[T_{c1}\left(x,0\right)\quad T_{c2}\left(x,0\right)\right]$, $\overline{\mathbf{T}}_p\left(x,0\right)=\mathrm{diag}\left[T_{p1}\left(x,0\right)\quad T_{p2}\left(x,0\right)\right]$, and $\overline{\mathbf{T}}_c\left(l_{ce},0\right)=\mathrm{diag}\left[T_{c1}\left(l_{ce},0\right)\quad T_{c2}\left(l_{ce},0\right)\right]$.

The governing nonlinear PDEs of motion for the coupled double-cable hoisting system are derived from Hamilton's principle as follows:

$$\rho\hat{\mathbf{a}}-\hat{\mathbf{T}}-EA\hat{\boldsymbol{\varepsilon}}=\rho\hat{\mathbf{g}}, \tag{3.24}$$

with the related terms defined as

$$\hat{\mathbf{a}}=\begin{bmatrix}\ddot{\mathbf{u}}\\ \ddot{\mathbf{w}}\\ \ddot{\mathbf{v}}\end{bmatrix}+2V\begin{bmatrix}\dot{\mathbf{u}}'\\ \dot{\mathbf{w}}'\\ \dot{\mathbf{v}}'\end{bmatrix}+a\begin{bmatrix}\mathbf{u}'\\ \mathbf{w}'\\ \mathbf{v}'\end{bmatrix}+V^2\begin{bmatrix}\mathbf{u}''\\ \mathbf{w}''\\ \mathbf{v}''\end{bmatrix}+a\begin{bmatrix}\mathbf{I}_4\\ \mathbf{0}_4\\ \mathbf{0}_4\end{bmatrix},\quad \hat{\mathbf{T}}=\begin{bmatrix}\mathbf{I}_4 & \mathbf{0}_4 & \mathbf{0}_4\\ \mathbf{0}_4 & \overline{\mathbf{w}}' & \mathbf{0}_4\\ \mathbf{0}_4 & \mathbf{0}_4 & \overline{\mathbf{v}}'\end{bmatrix}\begin{bmatrix}\mathbf{T}'\\ \mathbf{T}'\\ \mathbf{T}'\end{bmatrix}+\begin{bmatrix}\mathbf{0}_4 & \mathbf{0}_4 & \mathbf{0}_4\\ \mathbf{0}_4 & \overline{\mathbf{w}}'' & \mathbf{0}_4\\ \mathbf{0}_4 & \mathbf{0}_4 & \overline{\mathbf{v}}''\end{bmatrix}\begin{bmatrix}\mathbf{T}\\ \mathbf{T}\\ \mathbf{T}\end{bmatrix},$$

$$\hat{\boldsymbol{\varepsilon}}=\begin{bmatrix}\mathbf{I}_4 & \mathbf{0}_4 & \mathbf{0}_4\\ \mathbf{0}_4 & \overline{\mathbf{w}}' & \mathbf{0}_4\\ \mathbf{0}_4 & \mathbf{0}_4 & \overline{\mathbf{v}}'\end{bmatrix}\begin{bmatrix}\boldsymbol{\varepsilon}'\\ \boldsymbol{\varepsilon}'\\ \boldsymbol{\varepsilon}'\end{bmatrix}+\begin{bmatrix}\mathbf{0}_4 & \mathbf{0}_4 & \mathbf{0}_4\\ \mathbf{0}_4 & \overline{\mathbf{w}}'' & \mathbf{0}_4\\ \mathbf{0}_4 & \mathbf{0}_4 & \overline{\mathbf{v}}''\end{bmatrix}\begin{bmatrix}\boldsymbol{\varepsilon}\\ \boldsymbol{\varepsilon}\\ \boldsymbol{\varepsilon}\end{bmatrix},\quad \hat{\mathbf{g}}=g\left[\sin\theta\quad \sin\theta\quad 1\quad 1\quad 0\quad 0\quad 0\quad 0\quad 0\quad 0\quad 0\quad 0\right]^{\mathrm{T}},$$

where $\mathbf{I}_4$ is the 4×4 identity matrix, and $\mathbf{0}_4$ is a four-dimensional zero column vector.

The terms $\hat{\mathbf{T}}$ and $\hat{\boldsymbol{\varepsilon}}$ shown above represent the dynamic coupling forces and elastic strains, respectively, arising from three-dimensional interactions among tension, strain, and vibration.

The boundary conditions at the drum, guide-pulley, and cage interfaces are prescribed as follows:

$$\left(\frac{I_d}{R_d^2}+\rho\left(\overline{\mathbf{l}}_p\left(0\right)-\overline{\mathbf{l}}_p\right)\right)\left(\ddot{\mathbf{u}}_c+2V\dot{\mathbf{u}}_c'+a\mathbf{u}_c'+V^2\mathbf{u}_c''+a\right)+EA\boldsymbol{\varepsilon}_c\left(l_{cb},t\right)+\mathbf{T}_c\left(l_{cb},t\right)=0, \tag{3.25}$$

$$\begin{aligned}&\frac{I_h}{R_h^2}\left(\ddot{\mathbf{u}}_p+2V\dot{\mathbf{u}}_p'+a\mathbf{u}_p'+V^2\mathbf{u}_p''+a\right)-c_h\left(V+\dot{\mathbf{u}}_c\left(l_{ce},t\right)\right)\\&+EA\left(\boldsymbol{\varepsilon}_c\left(l_{ce},t\right)-\boldsymbol{\varepsilon}_p\left(l_{pb},t\right)\right)+\left(\mathbf{T}_c\left(l_{ce},t\right)-\mathbf{T}_p\left(l_{pb},t\right)\right)=0\end{aligned}, \tag{3.26}$$

$$\begin{cases}ma_{yr}+\sum_{k=1}^{2}\left(T_{pk}+EA\varepsilon_{pk}\right)-mg=0\\ \dfrac{I_p}{h}\ddot{\theta}-k_p\sum_{k=1}^{2}S_k\theta-mg\cos\theta=0\\ ma_{xr}+\sum_{k=1}^{2}\left(T_{pk}w_{pk}'+EA\varepsilon_{pk}w_{pk}'\right)-c_d\sum_{k=1}^{2}\dot{S}_k-k_p\sum_{k=1}^{2}S_k=0\end{cases}, \tag{3.27}$$

where $\bar{\mathbf{l}}_p(0)=\mathrm{diag}\left[l_{p1}(0)\quad l_{p2}(0)\right]$ and $\bar{\mathbf{l}}_p=\mathrm{diag}\left[l_{p1}\quad l_{p2}\right]$.

4. Discretization of the equations of motion

To transform the governing nonlinear PDEs into a solvable system of ODEs, the Galerkin method is used for spatial discretization. In this system, the inclined strings have constant lengths, whereas the suspension-string lengths vary with time. To facilitate analysis of the time-varying segments, a dimensionless coordinate $\psi = x/l(t)$ is introduced. This transformation maps the time-dependent physical domain $x \in [0, l(t)]$ onto a fixed computational domain $\psi \in [0, 1]$. Consequently, the vibration displacements are reformulated in the new coordinate system as follows:

$$\begin{cases}u_{ck}(x,t)=u_{ck}(\psi,t),w_{ck}(x,t)=w_{ck}(\psi,t),v_{ck}(x,t)=v_{ck}(\psi,t)\\u_{pk}(x,t)=u_{pk}(\psi,t),w_{pk}(x,t)=w_{pk}(\psi,t),v_{pk}(x,t)=v_{pk}(\psi,t)\end{cases}. \tag{4.1}$$

After coordinate normalization, the cable vibration displacements are approximated as follows:

$$\begin{cases}u_{ck}(\psi,t)=\sum_{i=1}^{n}\phi_{ck,i}(\psi)q_{uck,i}(t),w_{ck}(\psi,t)=\sum_{i=1}^{n}\varphi_{ck,i}(\psi)q_{wck,i}(t)\\v_{ck}(\psi,t)=\sum_{i=1}^{n}\xi_{ck,i}(\psi)q_{vck,i}(t)\\u_{pk}(\psi,t)=\sum_{i=1}^{n}\phi_{pk,i}(\psi)q_{upk,i}(t)+\dfrac{1}{e^{c_h\beta_h}}\sum_{i=1}^{n}\phi_{ck,i}(1)q_{uck,i}(t)\\w_{pk}(\psi,t)=\sum_{i=1}^{n}\varphi_{pk,i}(\psi)q_{wpk,i}(t),v_{pk}(\psi,t)=\sum_{i=1}^{n}\xi_{pk,i}(\psi)q_{vpk,i}(t)\end{cases}, \tag{4.2}$$

where n denotes the modal truncation order; $q_{uck,i}(t)$, $q_{wck,i}(t)$, $q_{vck,i}(t)$, $q_{upk,i}(t)$, $q_{wpk,i}(t)$, and $q_{vpk,i}(t)$ are the generalized coordinates of the k-th cable, and $\phi_{ck,i}(\psi)$, $\varphi_{ck,i}(\psi)$, $\xi_{ck,i}(\psi)$, $\phi_{pk,i}(\psi)$, $\varphi_{pk,i}(\psi)$, and $\xi_{pk,i}(\psi)$ are the corresponding spatial trial functions, respectively.

Because a dimensionless coordinate is introduced, the partial derivatives in the original equations of motion must be transformed using the chain rule. The transformed derivatives for the inclined and suspension strings are given, respectively, by

$$\begin{cases} u_{x,ck} = \dfrac{1}{l_{ck}} \sum_{i=1}^{n} \phi'_{ck,i} q_{uck,i},\ u_{xx,ck}\left(x,t\right) = \dfrac{1}{l_{ck}^2} \sum_{i=1}^{n} \phi''_{ck,i} q_{uck,i},\ u_{xt,ck} = \dfrac{1}{l_{ck}} \sum_{i=1}^{n} \phi'_{ck,i} \dot{q}_{uck,i} \\ u_{t,ck} = \sum_{i=1}^{n} \phi_{ck,i} \dot{q}_{uck,i},\ u_{tt,ck} = \sum_{i=1}^{n} \phi_{ck,i} \ddot{q}_{uck,i} \end{cases}, \tag{4.3}$$

$$\begin{cases} w_{x,ck} = \dfrac{1}{l_{ck}} \sum_{i=1}^{n} \varphi'_{ck,i} q_{wck,i},\ w_{xx,ck}\left(x,t\right) = \dfrac{1}{l_{ck}^2} \sum_{i=1}^{n} \varphi''_{ck,i} q_{wck,i},\ w_{xt,ck} = \dfrac{1}{l_{ck}} \sum_{i=1}^{n} \varphi'_{ck,i} \dot{q}_{wck,i} \\ w_{t,ck} = \sum_{i=1}^{n} \varphi_{ck,i} \dot{q}_{wck,i},\ w_{tt,ck} = \sum_{i=1}^{n} \varphi_{ck,i} \ddot{q}_{wck,i} \end{cases}, \tag{4.4}$$

$$\begin{cases} v_{x,ck} = \dfrac{1}{l_{ck}} \sum_{i=1}^{n} \xi'_{ck,i} q_{vck,i},\ v_{xx,ck}\left(x,t\right) = \dfrac{1}{l_{ck}^2} \sum_{i=1}^{n} \xi''_{ck,i} q_{vck,i}, v_{xt,ck} = \dfrac{1}{l_{ck}} \sum_{i=1}^{n} \xi'_{ck,i} \dot{q}_{vck,i} \\ v_{t,ck} = \sum_{i=1}^{n} \xi_{ck,i} \dot{q}_{vck,i},\ v_{tt,ck} = \sum_{i=1}^{n} \xi_{ck,i} \ddot{q}_{vck,i} \end{cases}. \tag{4.5}$$

$$\begin{cases} u_{x,pk} = \dfrac{1}{l_{pk}} \sum_{i=1}^{n} \phi'_{pk,i} q_{upk,i},\ u_{xx,pk} = \dfrac{1}{l_{pk}^2} \sum_{i=1}^{n} \phi''_{pk,i} q_{upk,i} \\ u_{t,pk} = \sum_{i=1}^{n} \phi_{pk,i} \dot{q}_{upk,i} - \dfrac{\dot{l}_{pk}\psi}{l_{pk}} \sum_{i=1}^{n} \phi'_{pk,i} q_{upk,i} + \dfrac{1}{p} \sum_{i=1}^{n} \phi_{ck,i}\left(1\right) \dot{q}_{uck,i} \\ u_{xt,pk} = \dfrac{1}{l_{pk}} \sum_{i=1}^{n} \phi'_{pk,i} \dot{q}_{upk,i} - \dfrac{\dot{l}_{pk}}{l_{pk}^2} \sum_{i=1}^{n} \phi'_{pk,i} q_{upk,i} - \dfrac{\dot{l}_{pk}\psi}{l_{pk}^2} \sum_{i=1}^{n} \phi''_{pk,i} q_{upk,i} \\ u_{tt,pk} = \sum_{i=1}^{n} \phi_{pk,i} \ddot{q}_{upk,i} - \dfrac{2\dot{l}_{pk}\psi}{l_{pk}} \sum_{i=1}^{n} \phi'_{pk,i} \dot{q}_{upk,i} + \left(\dfrac{\dot{l}_{pk}\psi}{l_{pk}}\right)^2 \sum_{i=1}^{n} \phi''_{pk,i} q_{upk,i} \\ \qquad + \dfrac{2\dot{l}_{pk}^2\psi}{l_{pk}^2} \sum_{i=1}^{n} \phi'_{pk,i} q_{upk,i} - \dfrac{\ddot{l}_{pk}\psi}{l_{pk}} \sum_{i=1}^{n} \phi'_{pk,i} q_{upk,i} + \dfrac{1}{p} \sum_{i=1}^{n} \phi_{ck,i}\left(1\right) \ddot{q}_{uck,i} \end{cases}, \tag{4.6}$$

$$\begin{cases} w_{x,pk} = \dfrac{1}{l_{pk}} \sum_{i=1}^{n} \varphi'_{pk,i} q_{wpk,i},\ w_{xt,pk} = \dfrac{1}{l_{pk}} \sum_{i=1}^{n} \varphi'_{pk,i} \dot{q}_{wpk,i} - \dfrac{\dot{l}_{pk}}{l_{pk}^2} \sum_{i=1}^{n} \varphi'_{pk,i} q_{wpk,i} - \dfrac{\dot{l}_{pk}\psi}{l_{pk}^2} \sum_{i=1}^{n} \varphi''_{pk,i} q_{wpk,i} \\ w_{xx,pk} = \dfrac{1}{l_{pk}^2} \sum_{i=1}^{n} \varphi''_{pk,i} q_{wpk,i},\ w_{t,pk} = \sum_{i=1}^{n} \varphi_{pk,i} \dot{q}_{wpk,i} - \dfrac{\dot{l}_{pk}\psi}{l_{pk}} \sum_{i=1}^{n} \varphi'_{pk,i} q_{wpk,i} \\ w_{tt,pk} = \sum_{i=1}^{n} \varphi_{pk,i} \ddot{q}_{wpk,i} - \dfrac{2\dot{l}_{pk}\psi}{l_{pk}} \sum_{i=1}^{n} \varphi'_{pk,i} \dot{q}_{wpk,i} + \left(\dfrac{\dot{l}_{pk}\psi}{l_{pk}}\right)^2 \sum_{i=1}^{n} \varphi''_{pk,i} q_{wpk,i} \\ \qquad + \left(\dfrac{2\dot{l}_{pk}^2\psi}{l_{pk}^2} - \dfrac{\ddot{l}_{pk}\psi}{l_{pk}}\right) \sum_{i=1}^{n} \varphi'_{pk,i} q_{wpk,i} \end{cases}, \tag{4.7}$$

$$\begin{cases} v_{x,pk}=\dfrac{1}{l_{pk}}\displaystyle\sum_{i=1}^{n}\xi'_{pk,i}q_{vpk,i},\ v_{xt,pk}=\dfrac{1}{l_{pk}}\sum_{i=1}^{n}\xi'_{pk,i}\dot{q}_{vpk,i}-\dfrac{\dot{l}_{pk}}{l_{pk}^{2}}\sum_{i=1}^{n}\xi'_{pk,i}q_{vpk,i}-\dfrac{\dot{l}_{pk}\psi}{l_{pk}^{2}}\sum_{i=1}^{n}\xi''_{pk,i}q_{vpk,i} \\ v_{xx,pk}=\dfrac{1}{l_{pk}^{2}}\displaystyle\sum_{i=1}^{n}\xi''_{pk,i}q_{vpk,i},\ v_{t,pk}=\sum_{i=1}^{n}\xi_{pk,i}\dot{q}_{vpk,i}-\dfrac{\dot{l}_{pk}\psi}{l_{pk}}\sum_{i=1}^{n}\xi'_{pk,i}q_{vpk,i} \\ v_{tt,pk}=\displaystyle\sum_{i=1}^{n}\xi_{pk,i}\ddot{q}_{vpk,i}-\dfrac{2\dot{l}_{pk}\psi}{l_{pk}}\sum_{i=1}^{n}\xi'_{pk,i}\dot{q}_{vpk,i}+\left(\dfrac{\dot{l}_{pk}\psi}{l_{pk}}\right)^{2}\sum_{i=1}^{n}\xi''_{pk,i}q_{vpk,i}+\left(\dfrac{2\dot{l}_{pk}^{2}\psi}{l_{pk}^{2}}-\dfrac{\ddot{l}_{pk}\psi}{l_{pk}}\right)\sum_{i=1}^{n}\xi'_{pk,i}q_{vpk,i} \end{cases}. \tag{4.8}$$

In Eqs (4.3)–(4.8), the subscripts t and x denote partial derivatives with respect to time t and the spatial coordinate x, respectively. Substituting Eqs (4.3)–(4.8) into the governing equation of motion, Eq (3.24), gives expressions that are subsequently weighted by $\phi_{ck,j}(\psi)$, $\varphi_{ck,j}(\psi)$, $\xi_{ck,j}(\psi)$, $\phi_{pk,j}(\psi)$, and $\varphi_{pk,j}(\psi)$, respectively, and integrated over the fixed computational domain $\psi \in [0, 1]$. Similarly, Eqs (4.3)–(4.8) are substituted into Eqs (3.25)–(3.27) and evaluated using the boundary weights $\phi_{ck,j}(1)$, $\varphi_{ck,j}(1)$, $\xi_{ck,j}(1)$, $\phi_{pk,j}(1)$, $\varphi_{pk,j}(1)$, and $\xi_{ck,j}(1)$, respectively, thereby completing the discretization. The governing nonlinear PDEs are thus reduced to the following ODE system for the double-cable hoist:

$$\begin{bmatrix} \mathbf{M}_u & 0 & 0 \\ 0 & \mathbf{M}_w & 0 \\ 0 & 0 & \mathbf{M}_v \end{bmatrix}\begin{bmatrix} \ddot{\mathbf{q}}_u \\ \ddot{\mathbf{q}}_w \\ \ddot{\mathbf{q}}_v \end{bmatrix}+\begin{bmatrix} \mathbf{C}_u & 0 & 0 \\ 0 & \mathbf{C}_w & 0 \\ 0 & 0 & \mathbf{C}_v \end{bmatrix}\begin{bmatrix} \dot{\mathbf{q}}_u \\ \dot{\mathbf{q}}_w \\ \dot{\mathbf{q}}_v \end{bmatrix}+\begin{bmatrix} \mathbf{K}_u & 0 & 0 \\ 0 & \mathbf{K}_w & 0 \\ 0 & 0 & \mathbf{K}_v \end{bmatrix}\begin{bmatrix} \mathbf{q}_u \\ \mathbf{q}_w \\ \mathbf{q}_v \end{bmatrix}=\begin{bmatrix} \mathbf{P}_u \\ \mathbf{P}_w \\ \mathbf{P}_v \end{bmatrix}+\begin{bmatrix} \mathbf{F}_u \\ \mathbf{F}_w \\ \mathbf{F}_v \end{bmatrix}, \tag{4.9}$$

where $\mathbf{M}_r$, $\mathbf{C}_r$, and $\mathbf{K}_r$ ($r = u, w, v$) denote the mass, damping, and stiffness matrices, respectively, $\mathbf{q}_r$ represents the generalized coordinate vector, $\mathbf{P}_r$ denotes the coupling terms induced by three-dimensional cable-vibration interactions, and $\mathbf{F}_r$ is the corresponding generalized force vector. The detailed formulations of these matrices and vectors are provided in the Appendix.

Solving Eq (4.9) yields the generalized coordinates associated with the three-dimensional cable vibrations. In this model, the guide-rail fault excitation $e(t)$ acts only in the transverse direction. Therefore, a nonhomogeneous cage-end boundary displacement is introduced only for the transverse displacement of the suspension string. The lateral displacement is not subjected to boundary excitation and still satisfies homogeneous boundary conditions.

Accordingly, the transverse displacement of the suspension string is expressed as the sum of a lifting term and a relative vibration component, while the lateral displacement is directly expanded by sine trial functions. By modeling the cables as flexible axially moving strings, the corresponding spatial trial functions are written as follows:

$$\begin{cases} \phi_{ck,i}(\psi)=\phi_{pk,i}(\psi)=\sqrt{2}\sin\left(\dfrac{2i-1}{2}\pi\psi\right) \\ \varphi_{ck,i}(\psi)=\varphi_{pk,i}(\psi)=\sqrt{2}\sin(i\pi\psi) \\ \xi_{ck,i}(\psi)=\xi_{pk,i}(\psi)=\sqrt{2}\sin(i\pi\psi) \end{cases} \quad i=1,2,\cdots,n. \tag{4.10}$$

In Eq (4.10), the sine functions for the transverse and lateral directions are used for the relative vibration displacements after removing the cage-end boundary motion. Therefore, although these functions vanish at both ends, they are compatible with the nonzero cage-end displacement through the lifting function introduced below.

Substituting the generalized coordinates and spatial trial functions into Eqs (4.1) and (4.2) gives the coupled longitudinal, transverse, and lateral vibration displacements of the cables as follows:

$$\begin{cases} u_{ck}(x,t)=\sum_{i=1}^{n}\sqrt{2}\sin\left(\frac{(2i-1)\pi}{2}\frac{x_c}{l_c}\right)q_{uck,i}(t) \\ w_{ck}(x,t)=\sum_{i=1}^{n}\sqrt{2}\sin\left(i\pi\frac{x_c}{l_c}\right)q_{wck,i}(t) \\ v_{ck}(x,t)=\sum_{i=1}^{n}\sqrt{2}\sin\left(i\pi\frac{x_c}{l_c}\right)q_{vck,i}(t) \end{cases}, \tag{4.11}$$

$$\begin{cases} u_{pk}(x,t)=\sum_{i=1}^{n}\sqrt{2}\sin\left(\frac{(2i-1)\pi}{2}\frac{x_p}{l_p}\right)q_{upk,i}(t)+\frac{1}{e^{c_h\beta_h}}\sum_{i=1}^{n}\sqrt{2}\sin\left(\frac{(2i-1)\pi}{2}\right)q_{uck,i}(t) \\ w_{pk}(x,t)=\frac{x_p}{l_p}w_{g,pk}(t)+\sum_{i=1}^{n}\sqrt{2}\sin\left(i\pi\frac{x_p}{l_p}\right)q_{wpk,i}(t) \\ v_{pk}(x,t)=\sum_{i=1}^{n}\sqrt{2}\sin\left(i\pi\frac{x_p}{l_p}\right)q_{vpk,i}(t) \end{cases}, \tag{4.12}$$

where $w_{g,pk}(t)$ denote the transverse displacements of the cage-end attachment point of the k-th cable segment. This is determined by the transverse cage motion induced by the guide-rail fault $e(t)$. This displacement is not expanded by the sine trial functions. Instead, it is introduced through the lifting term, so that the transverse displacement of the suspension string can satisfy the nonzero cage-end boundary condition.

The total tension in each hoisting cable consists of static and dynamic components and is expressed as follows:

$$\mathbf{T}_d=\mathbf{m}g+\rho g\mathbf{l}+\mu_e k_p\mathbf{S}+EA\left(\mathbf{u}'+\frac{1}{2}\overline{\mathbf{w}}'\cdot\mathbf{w}'+\frac{1}{2}\overline{\mathbf{v}}'\cdot\mathbf{v}'\right). \tag{4.13}$$

The tension difference between the coupled cables is defined as follows:

$$\Delta T_d=\frac{\left|T_{d1}-T_{d2}\right|}{\left(\frac{T_{d1}+T_{d2}}{2}\right)}. \tag{4.14}$$

5. Numerical simulations

The physical and geometric parameters used in the numerical simulations of the double-cable hoisting system are summarized in Table 2.

The nonstationary dynamic responses of the hoisting system are evaluated during upward hoisting according to the prescribed motion profile shown in Figure 3. This motion pattern is used as a representative operating condition and is not intended to cover all possible working states of the double-cable hoisting system. In practical operation, the two suspension strings move synchronously with the cage during upward hoisting and downward lowering. In this study, we focus on the upward-hoisting response induced by rigid-guide deviations and guide-roller contact excitations. The rigid-guide deviations are introduced as boundary excitations acting on the suspension strings. Because these excitations mainly affect the suspension segments, in the following analysis, we focus on their nonstationary responses. Unless otherwise stated, every rigid-guide section is assumed to contain either a curvature or a verticality imperfection.

Table 2. System parameters used in the numerical simulations.

Parameters	Values	Parameters	Values
R_d (m)	2.5	k_g (N/m)	2.24×10^6
I_d (kg·m^2)	3×10^4	c_d (N·s/m)	1.4×10^4
R_h (m)	2.5	EI(N·m^2)	1.34×10^8
I_h (kg·m^2)	1.52×10^4	I_p (kg·m^2)	5.2×10^4
c_h	0.25	μ_e	0.1
β_h (rad)	0.75 π	$e_{c,\max}$ (m)	5×10^{-3}
EA (N)	2.09×10^8	$e_{p,\max}$ (m)	5×10^{-3}
ρ (kg/m)	8.53	l_g (m)	12
l_c (m)	80	h (m)	4.5
α (rad)	0.25 π	d_e (m)	15×10^{-3}
L_0 (m)	1538	s_1 (m)	2.5
a (m/s^2)	0.75	s_2 (m)	2.5
m (kg)	8.8×10^4	d (m)	2×10^{-3}
g (m/s^2)	9.8	k_r (N/m)	1.6×10^6

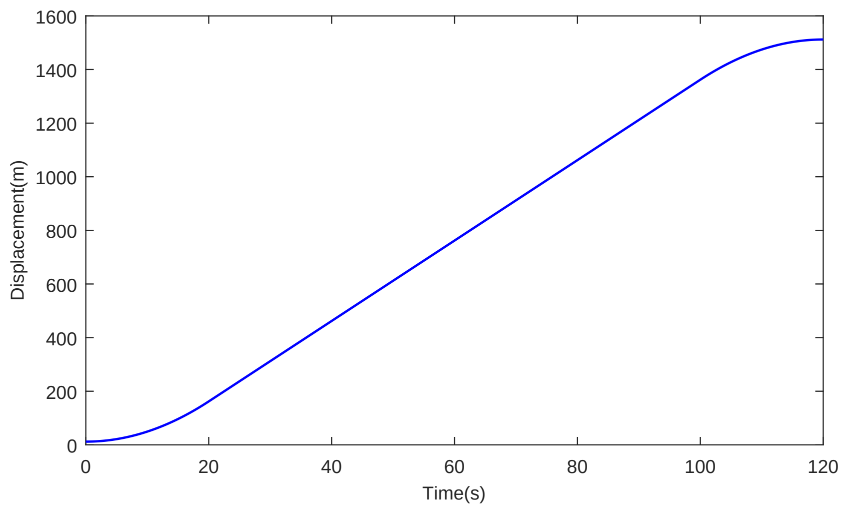

Figure 3. Representative upward-hoisting motion pattern of the coupled double-cable hoist.

5.1. Numerical implementation and verification

To improve the reproducibility and reliability of the numerical results, the numerical implementation was verified from three aspects: Galerkin modal convergence, time-step convergence, and a no-guide-deviation limiting case. The modal truncation order and time step were then fixed for the subsequent simulations involving curvature and verticality deviations.

The nonlinear ordinary differential equations obtained after Galerkin discretization was solved using a classical fourth-order explicit Runge-Kutta method with a fixed time step. Because a fixed-step explicit scheme was adopted, no adaptive time-step control or error tolerance was used. At each time-integration step, four Runge-Kutta stages were evaluated. The nonlinear contact force and time-varying coefficients were calculated from the displacement, velocity, and time values at the current stage. Accordingly, the unilateral contact terms were treated explicitly. When the contact condition was not satisfied, the contact force was set to zero; otherwise, the contact force was activated according to the prescribed nonlinear contact model.

The initial conditions were set as zero displacement and zero velocity for all generalized coordinates, corresponding to an unperturbed equilibrium state at t = 0. In the following numerical results, the response denoted at $l_p(t)/2$ was evaluated at the instantaneous midpoint of the suspension string in the physical coordinate, namely $x_p(t) = l_p(t)/2$. Equivalently, in the normalized coordinate, this point corresponds to $\psi = 1/2$. Because $l_p(t)/2$ varies with time during hoisting, the plotted response represents the instantaneous spatial midpoint of the current suspension-string span.

5.1.1. Galerkin modal convergence

To justify the modal truncation order used in the Galerkin discretization, a convergence study is conducted with respect to the number of retained modes. Truncation orders of n = 4, 6, and 8 are considered for the curvature-deviation and verticality-deviation cases.

Table 3. Convergence test with respect to the Galerkin modal truncation order for curvature deviation.

Truncation order n	$\Delta T_{\max}$ (kN)	Tension-inconsistency ratio (%)
4	42.7098	9.2442
6	43.3955	9.3894
8	43.6824	9.4392

Table 4. Convergence test with respect to the Galerkin modal truncation order for verticality deviation.

Truncation order n	$\Delta T_{\max}$ (kN)	Tension-inconsistency ratio (%)
4	36.9077	7.9980
6	37.4741	8.1192
8	37.6715	8.1606

As shown in Tables 3 and 4, the key response quantities, including the maximum tension difference and the maximum tension-inconsistency ratio, exhibit only minor variations as n increases. In particular, when the modal order increases from n = 6 to n = 8, the relative change in the maximum tension difference is less than 1%, indicating that the Galerkin solution has essentially converged. Therefore, n = 6 is adopted in the subsequent numerical simulations to balance computational efficiency and accuracy.

5.1.2. Time step convergence

In this numerical implementation, an explicit fixed-step integration scheme is adopted. Accordingly, no adaptive time-stepping strategy or error-tolerance control is introduced. The numerical accuracy is verified through a time-step convergence study.

Table 5. Time-step convergence of key response quantities for curvature deviation case.

Time step Δt (s)	$\Delta T_{\max}$ (kN)	Tension-inconsistency ratio (%)
4×10^{-4}	43.3781	9.3856
2×10^{-4}	43.3955	9.3894
1×10^{-4}	43.4030	9.3910

Table 6. Time-step convergence of key response quantities for verticality deviation case.

Time step Δt (s)	$\Delta T_{\max}$ (kN)	Tension-inconsistency ratio (%)
4×10^{-4}	37.4612	8.1164
2×10^{-4}	37.4741	8.1194
1×10^{-4}	37.4806	8.1208

As shown in Tables 5 and 6, three time steps, $\Delta t = 4 \times 10^{-4}$ s, 2×10^{-4} s, and 1×10^{-4} s, are tested for the curvature-deviation and verticality-deviation cases. The key response quantities change only slightly when the time step is reduced from 2×10^{-4} s to 1×10^{-4} s, confirming that further refinement of Δt has no significant influence on the numerical results. Therefore, $\Delta t = 2 \times 10^{-4}$ s is adopted in the subsequent simulations.

5.1.3. No-guide-deviation limiting case

To further verify the consistency of the proposed model, a no-guide-deviation case is considered a limiting-case benchmark. In this case, the curvature and verticality deviations are both set to zero, i.e., $e_c = e_p = 0$, thereby eliminating guide-deviation-induced contact excitation from the system.

Figure 4 shows the tension difference and tension-inconsistency ratio between the two suspension strings at $l_p(t)/2$ in the no-guide-deviation case. Both quantities remain close to zero throughout the hoisting process. Only slight fluctuations appear during the initial stage, mainly due to the transient response associated with the prescribed hoisting motion rather than guide-roller excitation. After this initial transient, the tension difference and tension-inconsistency ratio rapidly approach zero and remain nearly unchanged.

This result indicates that, in the absence of curvature and verticality deviations, the two suspension strings maintain nearly symmetric dynamic responses, and no artificial tension imbalance is introduced by the governing equations or numerical implementation. Therefore, the much larger tension inconsistency observed in the curvature- and verticality-deviation cases can be attributed to guide-deviation-induced contact excitation rather than numerical artifacts.

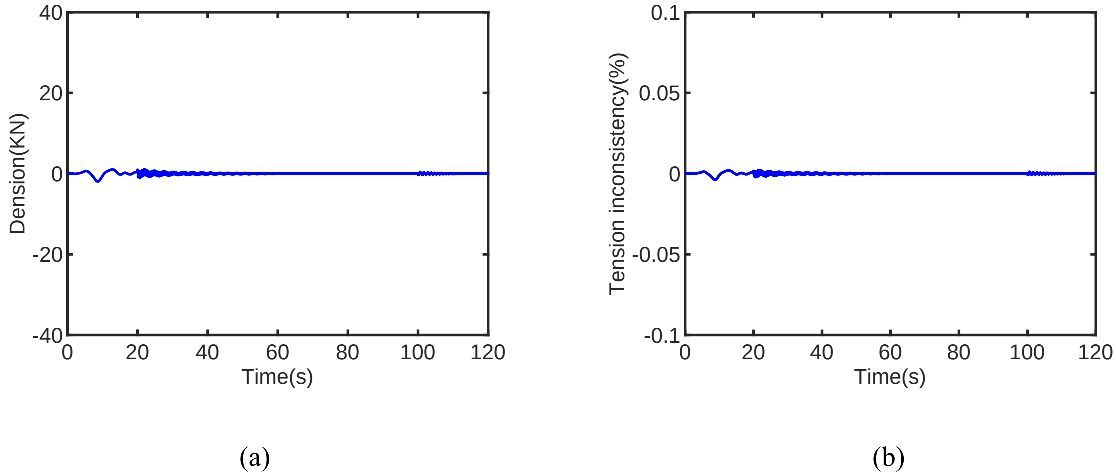

Figure 4. Tension inconsistency between the suspension strings at $l_p(t)/2$ in the no-guide-deviation case. (a) Tension difference. (b) Tension ratio.

5.2. Curvature deviation

Curvature deviations in the rigid guides, which are commonly caused by manufacturing or installation imperfections, may pose a substantial risk to hoisting systems. These geometric irregularities can degrade the operational stability of a double-cable hoist and may lead to severe faults, such as cable failure or guide-roller disengagement. The dynamic responses of the system under curvature deviations are shown in Figures 5–9.

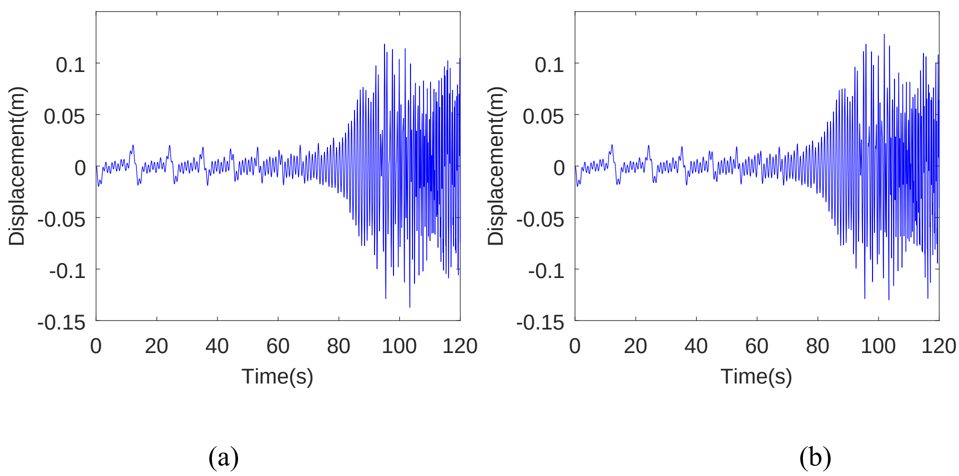

Figure 5. Transverse vibration displacements of the suspension strings at lp(t)/2 under curvature deviations. (a) String 1. (b) String 2.

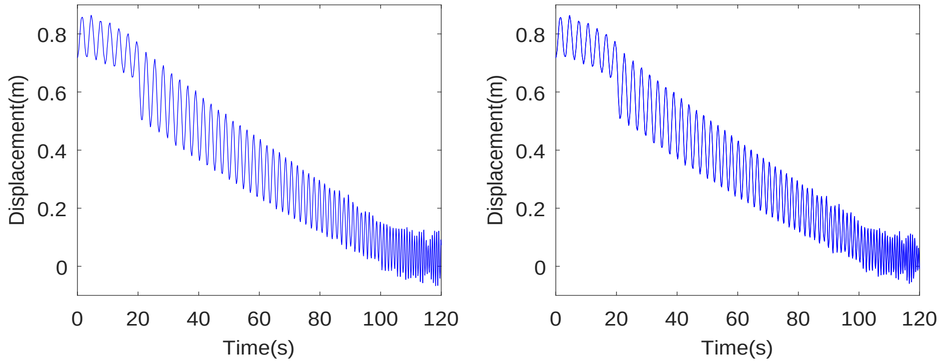

(a) (b)

Figure 6. Longitudinal vibration displacements of the suspension strings at lp(t)/2 under curvature deviations. (a) String 1. (b) String 2.

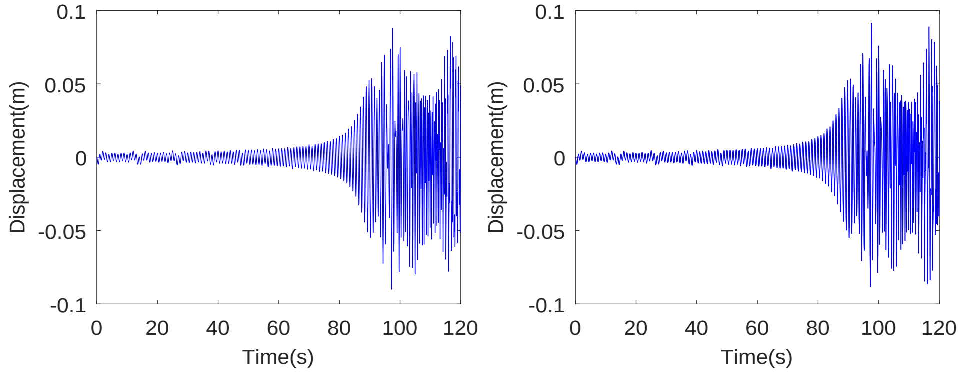

(a) (b)

Figure 7. Lateral vibration displacements of the suspension strings at lp(t)/2 under curvature deviations. (a) String 1. (b) String 2.

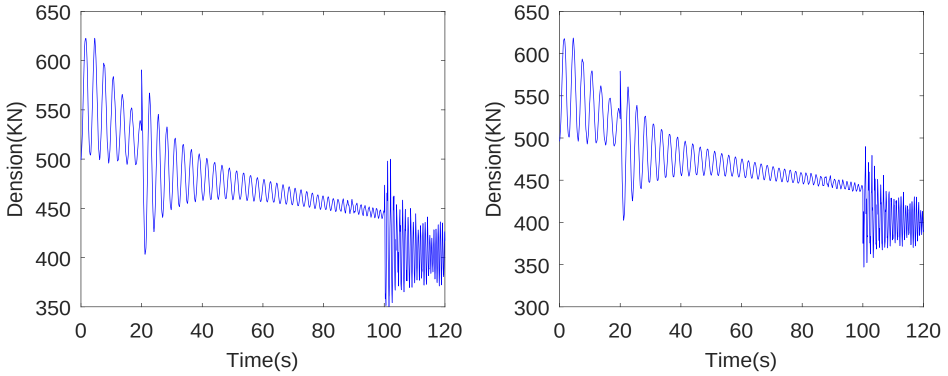

(a) (b)

Figure 8. Tensions of the suspension strings at lp(t)/2 under curvature deviations. (a) String 1. (b) String 2.

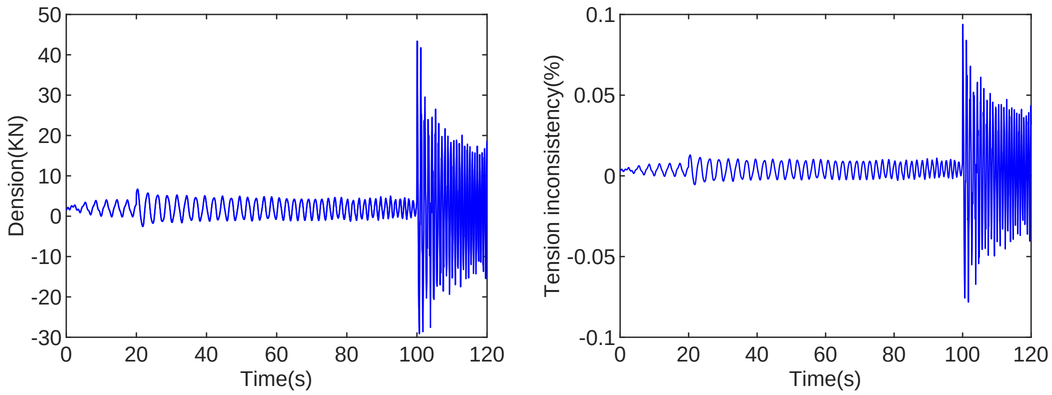

(a) (b)

Figure 9. Tension inconsistency between the suspension strings at lp(t)/2 under curvature deviations. (a) Tension difference. (b) Tension ratio.

As shown in Figure 5, string 1 exhibits a larger transverse vibrational displacement than string 2, indicating an asymmetric transverse response of the two parallel suspension strings under curvature deviations. This asymmetry mainly results from slight cage rotation caused by nonuniform contact forces from the rigid guides. The rotation changes the system geometry and static load distribution, thereby amplifying the vibration response of string 1. As the hoist moves upward, the amplitude and the frequency of the transverse vibration increase. This behavior is attributed to the continuous shortening of the suspension string length $l_p(t)$, which increases the equivalent transverse stiffness and frequencies of the system and promotes vibration-energy accumulation.

Figure 6 shows that the longitudinal vibration displacement of string 1 is slightly greater than that of string 2. This difference can be attributed to a small counterclockwise rotation of the cage under external perturbations, which shifts its geometric center. Consequently, the effective static length of string 1 becomes slightly greater than that of string 2, further affecting the dynamic characteristics and load distribution of the two cables. Overall, however, the longitudinal vibration displacements gradually decrease during upward hoisting. This reduction is governed by the shortening of the strings, because the decrease in static elongation caused by self-weight dominates the macroscopic longitudinal response.

Figure 7 indicates that string 1 also has a slightly larger lateral displacement than string 2. This difference arises from three-dimensional coupling and is consistent with the amplified transverse and longitudinal responses observed in string 1. As the hoist ascends, the time-varying length of the suspension strings increases the amplitude and frequency of the lateral response, following a trend similar to that of the transverse vibration.

Figure 8 shows that the total tension in string 1 is slightly higher than that in string 2. Because the cable tension is strongly affected by the three-dimensional coupled vibrations, the total tensions of both suspension strings generally decrease during upward motion. Pronounced tension fluctuations occur during the transient acceleration and deceleration stages.

As shown in Figure 9, the tension inconsistency between the suspension strings becomes more severe as the hoist ascends. This increase is mainly associated with the increasing multidirectional vibration frequencies during hoisting. The most unstable response occurs during deceleration, when the tension inconsistency exhibits pronounced fluctuations.

It should be noted that the reduction in transverse and lateral vibration amplitudes during the deceleration stage does not necessarily indicate a corresponding reduction in tension inconsistency between the two suspension strings. These quantities characterize different aspects of the system response. Specifically, the transverse and lateral vibration amplitudes mainly reflect the displacement response of the strings, whereas the tension-inconsistency ratio is governed by the combined effects of displacement, velocity, acceleration, contact force, and dynamic load redistribution between the two suspension strings. During deceleration, the time-varying string length and axial-velocity variation may partly suppress the transverse and lateral displacement envelopes. However, the inertial effect associated with deceleration, together with contact-induced excitation, can cause substantial redistribution of dynamic tension between the two strings. Consequently, the most pronounced tension inconsistency may occur during the deceleration stage, even when the transverse and lateral displacement amplitudes are partially reduced.

Table 7. Peak dynamic responses under curvature deviation.

String	$u_{\max}$ (m)	$w_{\max}$ (m)	$v_{\max}$ (m)	$T_{\max}$ (kN)	$\Delta T_{\max}$ (kN)	Tension-inconsistency ratio (%)
String 1	0.8642	0.1372	0.0914	622.8	43.40	9.389
String 2	0.8589	0.1287	0.0872	617.6		

To quantitatively characterize the curvature-deviation response, the peak displacement, cable tension, maximum tension difference, and tension-inconsistency ratio are summarized in Table 7. string 1 shows slightly larger peak displacement and tension responses than string 2, indicating an asymmetric dynamic response between the two suspension strings. The maximum tension difference reaches 43.40 kN, and the corresponding tension-inconsistency ratio is 9.389%. These results indicate that curvature-induced guide-roller excitation leads to noticeable dynamic load redistribution between the two suspension strings.

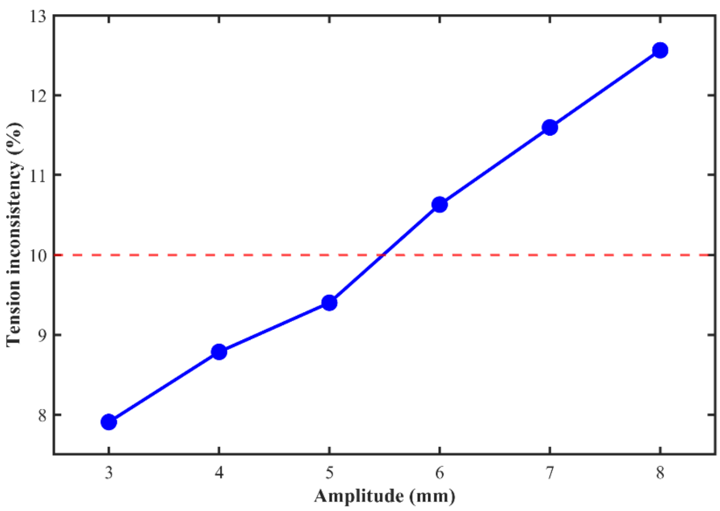

Figure 10. Tension inconsistency between the suspension strings at lp(t)/2 for different maximum curvature-deviation amplitudes.

Figure 10 shows that, for the double-cable hoisting system studied in this paper and under the parameters listed in Table 2, the maximum tension-inconsistency ratio exceeds the adopted 10% admissible criterion [43] when the maximum curvature-deviation amplitude $e_{c,\max}$ is greater than 6 mm. For the studied system, keeping the curvature-deviation amplitude below this value helps maintain the tension-inconsistency ratio within the adopted safety criterion.

5.3. Verticality deviation

Verticality deviations of the rigid guides are mainly caused by assembly and installation errors in hoisting systems. These deviations excite coupled transverse, longitudinal, and lateral vibrations of the suspension strings, which in turn produce tension inconsistency between the two parallel strings. The corresponding dynamic responses of the coupled double-cable hoist are shown in Figures 11–15.

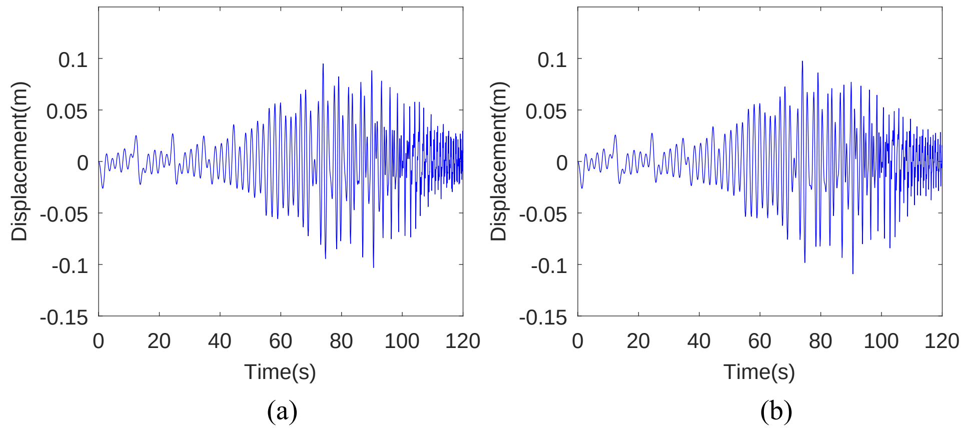

Figure 11. Transverse vibration displacements of the suspension strings at lp(t)/2 under verticality deviations. (a) String 1. (b) String 2.

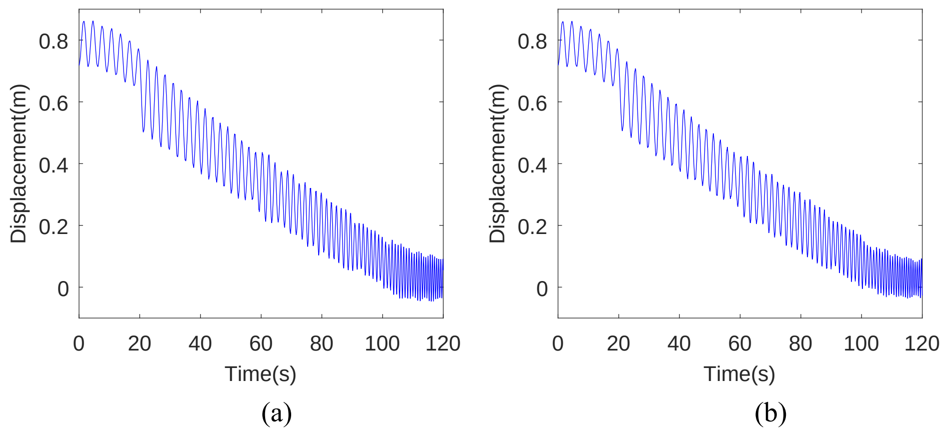

Figure 12. Longitudinal vibration displacements of the suspension strings at lp(t)/2 under verticality deviations. (a) String 1. (b) String 2.

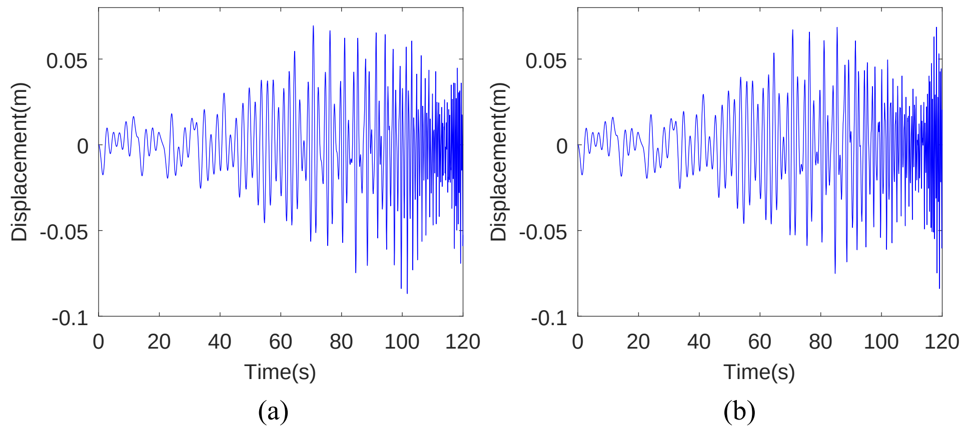

Figure 13. Lateral vibration displacements of the suspension strings at lp(t)/2 under verticality deviations. (a) String 1. (b) String 2.

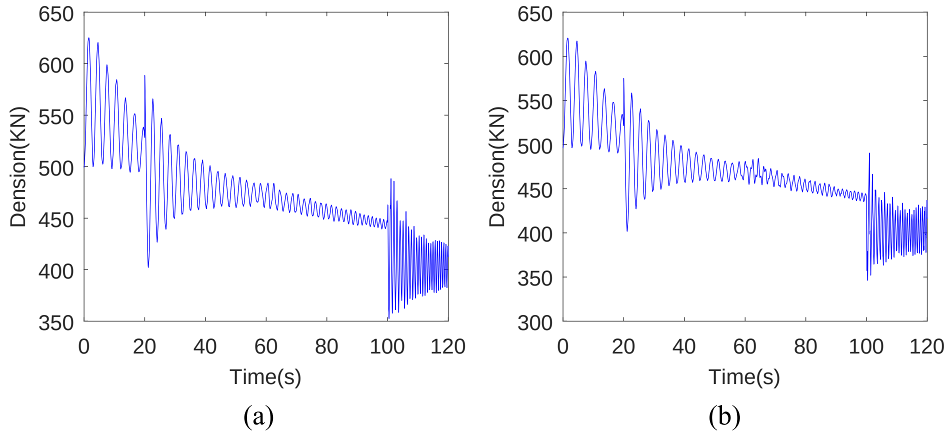

Figure 14. Tensions of the suspension strings at lp(t)/2 under verticality deviations. (a) String 1. (b) String 2.

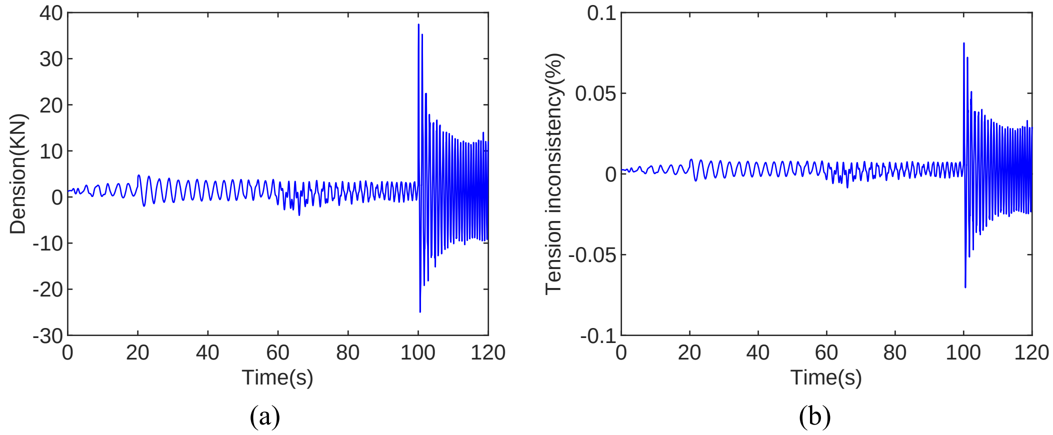

Figure 15. Tension inconsistency between the suspension strings at lp(t)/2 under verticality deviations. (a) Tension difference. (b) Tension ratio.

The dynamic behavior of the hoisting system under verticality deviations is broadly consistent with that observed under curvature deviations. Specifically, string 1 consistently shows slightly larger vibration displacements than string 2 in all three directions in Figures 11–13. In addition, as the hoist moves upward, the amplitudes and frequencies of the transverse and lateral vibrations increase, whereas the longitudinal vibrational displacement gradually decreases. Consistent with the displacement responses, Figure 14 shows that the dynamic tension in string 1 is also slightly higher than that in string 2. The total tensions decrease during upward motion but fluctuate markedly during variable-acceleration stages. As a result, the tension inconsistency between the two strings becomes more severe and exhibits pronounced fluctuations during these transient stages in Figure 15. The mechanisms underlying these phenomena are essentially the same as those discussed for curvature deviations.

Table 8. Peak dynamic responses under verticality deviation.

String	$u_{\max}$ (m)	$w_{\max}$ (m)	$v_{\max}$ (m)	$T_{\max}$ (kN)	$\Delta T_{\max}$ (kN)	Tension-inconsistency ratio (%)
String 1	0.8620	0.1032	0.08681	625.2	37.47	8.119
String 2	0.8593	0.0973	0.08274	620.5		

To provide a more quantitative interpretation of the verticality-deviation response, the peak values of displacement, cable tension, maximum tension difference, and tension-inconsistency ratio are summarized in Table 8. These results enable a direct comparison of the peak dynamic responses of the two suspension strings. String 1 shows slightly larger peak displacement and tension responses than string 2, indicating an asymmetric dynamic response under verticality deviation. The maximum tension difference reaches 37.47 kN, and the corresponding tension-inconsistency ratio is 8.119%.

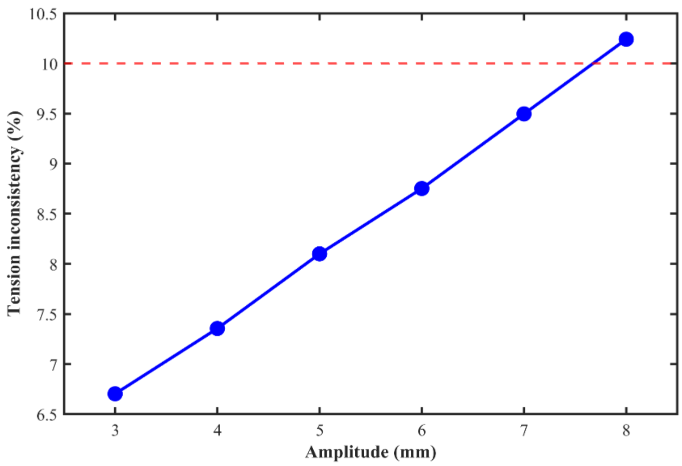

Figure 16. Tension inconsistency between the suspension strings at lp(t)/2 for different maximum verticality-deviation amplitudes.

From an operational-safety perspective, Figure 16 indicates that, for the studied hoisting system under the parameters listed in Table 2, the peak tension-inconsistency ratio exceeds the adopted 10% admissible criterion when the maximum verticality-deviation amplitude $e_{p,\max}$ is greater than 8 mm.

5.4. Comparative discussion and parameter sensitivity

The difference in tension inconsistency between curvature deviation and verticality deviation can be explained from the perspectives of contact-force evolution, cage motion, excitation pattern, and cable-coupling mechanism. Curvature deviation generates a continuously varying geometric excitation along each guide section, resulting in smooth but persistent guide–roller contact forces. This sustained excitation induces continuous cage rotation, thereby altering the effective boundary conditions of the two suspension strings. Consequently, the dynamic load is unevenly redistributed between the two cables, leading to a larger tension inconsistency. In contrast, verticality deviation is mainly concentrated near the transitions between adjacent guide sections and exhibits a localized, piecewise triangular excitation pattern. Although it can induce local vibration, its influence on sustained cage rotation and long-term cable coupling is weaker than that of curvature deviation. Therefore, under the same maximum deviation amplitude, the resulting tension inconsistency is smaller for verticality deviation.

To evaluate the system dependence of the predicted tension inconsistency, a parameter-sensitivity analysis is conducted for the roller stiffness k_r, contact damping coefficient c_d, guide clearance d_e, hoisting speed V, cage mass m, and hoisting displacement H. The maximum tension difference ΔT_{max} and the tension-inconsistency ratio are selected as the major evaluation indices. The sensitivity results for the curvature- and verticality-deviation cases are shown in Figures 17 and 18, respectively.

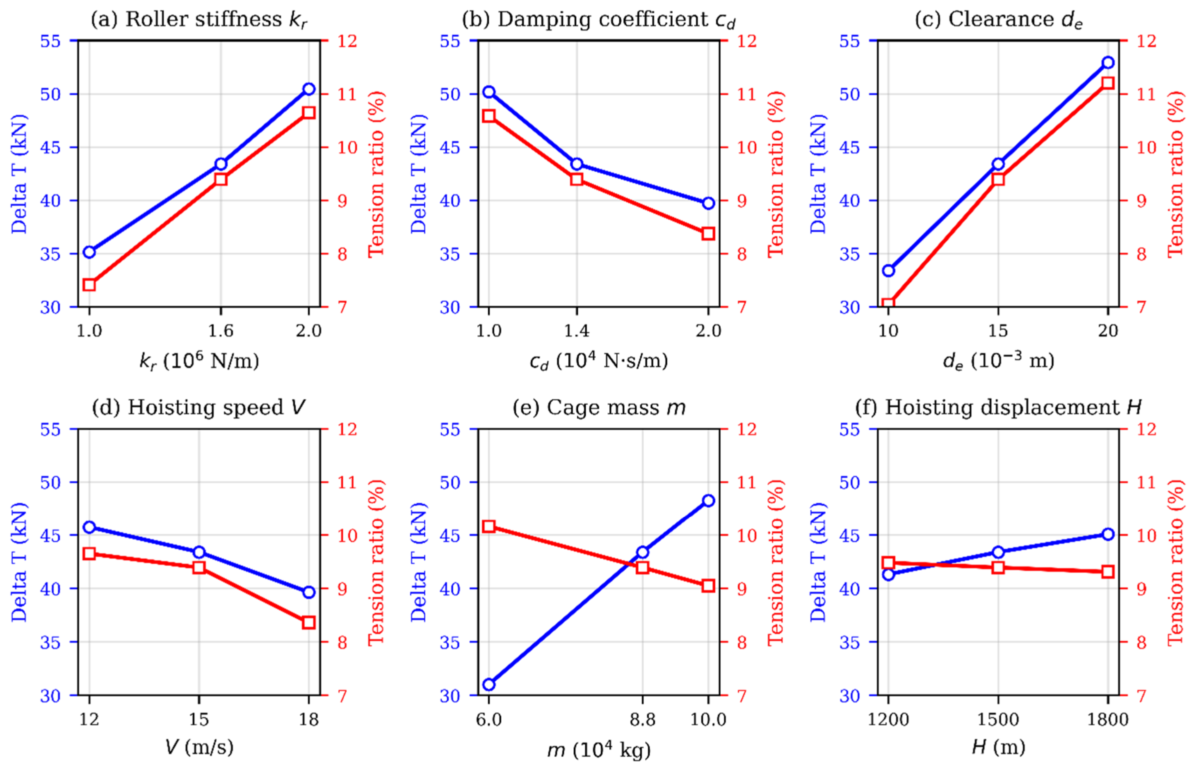

Figure 17. Sensitivity analysis of key parameters under curvature deviation.

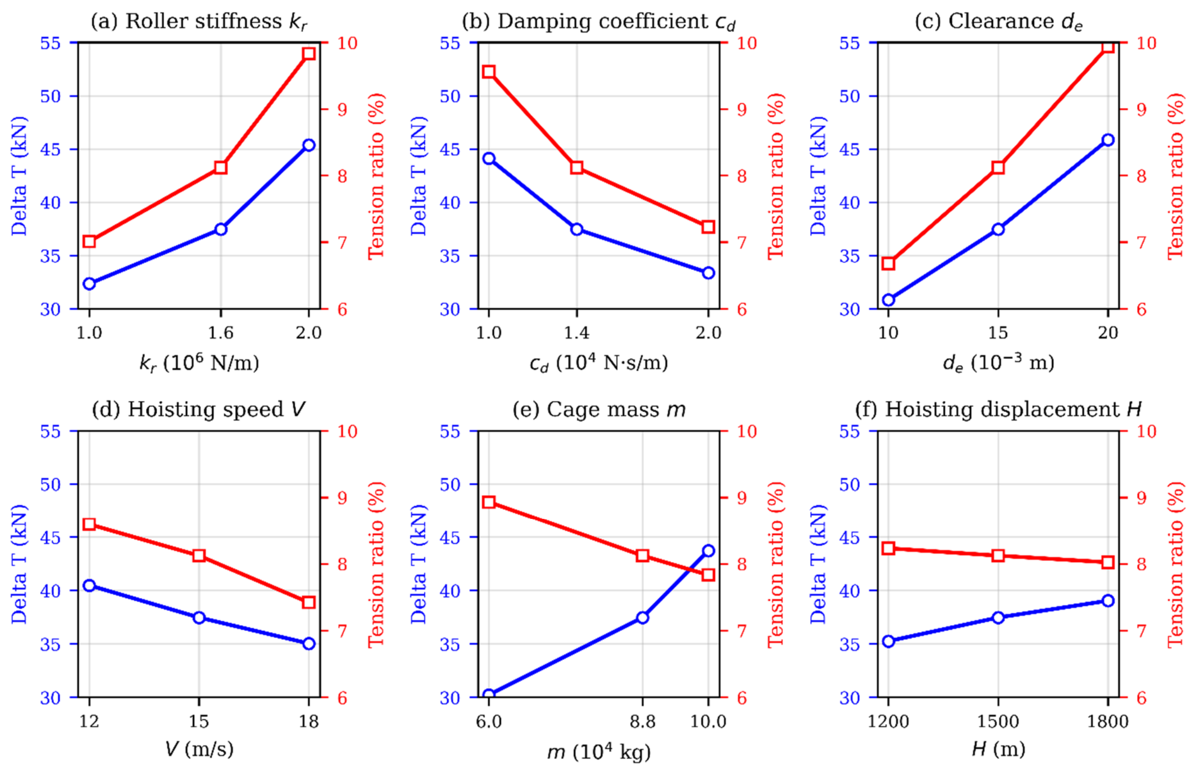

Figure 18. Sensitivity analysis of key parameters under verticality deviation.

The sensitivity results show that increasing the roller stiffness and guide clearance generally increases the tension difference and the tension-inconsistency ratio, whereas increasing the contact damping coefficient tends to suppress tension fluctuations. The effects of hoisting speed, cage mass, and hoisting displacement are more closely related to changes in the average cable tension and variations in the frequencies of the system. These results further confirm that the deviation-amplitude reference values identified in this study are system-specific and should be interpreted together with the parameter set listed in Table 2.

6. Conclusions

In this paper, a coupled dynamic model is developed for double-cable mine hoists subjected to rigid guide-roller contact excitations, and the nonstationary vibration responses induced by curvature and verticality deviations of the rigid guides are analyzed systematically. The major conclusions are summarized as follows:

1). The cable vibrations exhibit pronounced nonstationary characteristics during upward hoisting. The transverse and lateral displacement amplitudes increase during the early stage of upward motion and are partly suppressed during the deceleration stage, mostly because of the time-varying cable length and the resulting variation in system stiffness. In contrast, the longitudinal vibration decreases monotonically, primarily because the static elongation of the shortening cables gradually diminishes.

2). The tension inconsistency between the two suspension strings increases during upward motion under curvature and verticality deviations. It also fluctuates markedly during variable-acceleration stages, especially during deceleration. This observation is not contradictory to the partial suppression of transverse and lateral displacement amplitudes during deceleration, because the tension inconsistency is governed not only by displacement amplitude but also by velocity, acceleration, contact force, and dynamic load redistribution between the two suspension strings.

3). The harmonic excitation associated with curvature deviation is more likely to induce coupled vibrations. Consequently, for the same deviation amplitude, the resulting tension inconsistency is significantly larger than that caused by verticality deviation. For the studied double-cable hoisting system under the considered operating conditions, the maximum tension-inconsistency ratio exceeds the adopted 10% admissible criterion when the curvature-deviation amplitude is larger than 6 mm or when the verticality-deviation amplitude is larger than 8 mm. These values are system-specific reference amplitudes obtained from this numerical model and should not be regarded as universal design limits for all hoisting systems.

These results provide a useful basis for predicting the nonstationary vibration behavior of double-cable hoists and offer practical guidance for the safe design and operation of vertical transportation systems. Future work should include experimental or field validation and further refinement of the guide-roller contact model.

Use of AI tools declaration

The authors declare they have not used Artificial Intelligence (AI) tools in the creation of this article.

Acknowledgments

This work is partly supported by the Shandong Key Laboratory of Intelligent Manufacturing Technology for Advanced Power Equipment.

Conflict of interest

The authors declare there is no conflict of interest.

References

1. Y. Wang, G. Cao, W. T. van Horssen, Dynamic simulation of a multi-cable driven parallel suspension platform with slack cables, *Mech. Mach. Theory*, **126** (2018), 329–343. https://doi.org/10.1016/j.mechmachtheory.2018.04.014
2. J. Wang, Y. Pi, Y. Hu, X. Gong, Modeling and dynamic behavior analysis of a coupled multi-cable double drum winding hoister with flexible guides, *Mech. Mach. Theory*, **108** (2017), 191–208. https://doi.org/10.1016/j.mechmachtheory.2016.10.021
3. J. González-Carbajal, An analytical model for the drum-rope interaction in hoisting mechanisms and cable-driven systems, *Mech. Mach. Theory*, **207** (2025), 105939. https://doi.org/10.1016/j.mechmachtheory.2025.105939
4. R. S. Crespo, S. Kaczmarczyk, P. Picton, H. Su, Modelling and simulation of a stationary high-rise elevator system to predict the dynamic interactions between its components, *Int. J. Mech. Sci.*, **137** (2018), 24–45. https://doi.org/10.1016/j.ijmecsci.2018.01.011

5. D. Giagopoulos, I. Chatziparasidis, N. S. Sapidis, Dynamic and structural integrity analysis of a complete elevator system through a mixed computational-experimental finite element methodology, *Eng. Struct.*, **160** (2018), 473–487. https://doi.org/10.1016/j.engstruct.2018.01.018
6. M. J. Maghsoudi, Z. Mohamed, S. Sudin, S. Buyamin, H. I. Jaafar, S. M. Ahmad, An improved input shaping design for an efficient sway control of a nonlinear 3D overhead crane with friction, *Mech. Syst. Signal Process.*, **92** (2017), 364–378. https://doi.org/10.1016/j.ymssp.2017.01.036
7. R. Miranda-Colorado, L. T. Aguilar, A family of anti-swing motion controllers for 2D-cranes with load hoisting/lowering, *Mech. Syst. Signal Process.*, **133** (2019), 106253. https://doi.org/10.1016/j.ymssp.2019.106253
8. W. D. Zhu, G. Y. Xu, Vibration of elevator cables with small bending stiffness, *J. Sound Vib.*, **263** (2003), 679–699. https://doi.org/10.1016/S0022-460X(02)01468-2
9. S. Kaczmarczyk, R. Iwankiewicz, Gaussian and non-gaussian stochastic response of slender continua with time-varying length deployed in tall structures, *Int. J. Mech. Sci.*, **134** (2017), 500–510. https://doi.org/10.1016/j.ijmecsci.2017.10.030
10. W. D. Zhu, H. Ren, An accurate spatial discretization and substructure method with application to moving elevator cable-car systems–Part I: Methodology, *J. Vib. Acoust.*, **135** (2013), 051036. https://doi.org/10.1115/1.4024557
11. H. Ren, W. D. Zhu, An accurate spatial discretization and substructure method with application to moving elevator cable-car systems–Part II: Application, *J. Vib. Acoust.*, **135** (2013), 051037. https://doi.org/10.1115/1.4024558
12. D. H. Yang, K. Y. Kim, M. K. Kwak, S. Lee, Dynamic modeling and experiments on the coupled vibrations of building and elevator ropes, *J. Sound Vib.*, **390** (2017), 164–191. https://doi.org/10.1016/j.jsv.2016.10.045
13. W. D. Zhu, H. Ren, C. Xiao, A nonlinear model of a slack cable with bending stiffness and moving ends with application to elevator traveling and compensation cables, *J. Appl. Mech.*, **78** (2011), 041017. https://doi.org/10.1115/1.4003348
14. S. Kaczmarczyk, W. Ostachowicz, Transient vibration phenomena in deep mine hoisting cables. Part 1: Mathematical model, *J. Sound Vib.*, **262** (2003), 219–244. https://doi.org/10.1016/S0022-460X(02)01137-9
15. S. Kaczmarczyk, W. Ostachowicz, Transient vibration phenomena in deep mine hoisting cables. Part 2: Numerical simulation of the dynamic response, *J. Sound Vib.*, **262** (2003), 245–289. https://doi.org/10.1016/S0022-460X(02)01148-3
16. S. N. Gavrilov, E. V. Shishkina, Y. A. Mochalova, Non-stationary localized oscillations of an infinite string, with time-varying tension, lying on the Winkler foundation with a point elastic inhomogeneity, *Nonlinear Dyn.*, **95** (2019), 2995–3004. https://doi.org/10.1007/s11071-018-04735-3
17. X. Y. Mao, H. Ding, L. Q. Chen, Vibration of flexible structures under nonlinear boundary conditions, *J. Appl. Mech.*, **84** (2017), 111006. https://doi.org/10.1115/1.4037883
18. S. Lenci, F. Clementi, C. E. N. Mazzilli, Simple formulas for the natural frequencies of non-uniform cables and beams, *Int. J. Mech. Sci.*, **77** (2013), 155–163. https://doi.org/10.1016/j.ijmecsci.2013.09.028
19. T. Akkaya, W. T. van Horssen, Reflection and damping properties for semi-infinite string equations with non-classical boundary conditions, *J. Sound Vib.*, **336** (2015), 179–190. https://doi.org/10.1016/j.jsv.2014.10.014

20. L. Q. Chen, Y. Q. Tang, J. W. Zu, Nonlinear transverse vibration of axially accelerating strings with exact internal resonances and longitudinally varying tensions, *Nonlinear Dyn.*, **76** (2014), 1443–1468. https://doi.org/10.1007/s11071-013-1220-1
21. L. Q. Chen, W. J. Zhao, A numerical method for simulating transverse vibrations of an axially moving string, *Appl. Math. Comput.*, **160** (2005), 411–422. https://doi.org/10.1016/j.amc.2003.11.012
22. F. Nudo, A general quadratic enrichment of the Crouzeix–Raviart finite element, *J. Comput. Appl. Math.*, **451** (2024), 116112. https://doi.org/10.1016/j.cam.2024.116112
23. F. Nudo, Two one-parameter families of nonconforming enrichments of the Crouzeix–Raviart finite element, *Appl. Numer. Math.*, **203** (2024), 160–172. https://doi.org/10.1016/j.apnum.2024.05.023
24. F. Dell'Accio, A. Guessab, F. Nudo, New quadratic and cubic polynomial enrichments of the Crouzeix–Raviart finite element, *Comput. Math. Appl.*, **170** (2024), 204–212. https://doi.org/10.1016/j.camwa.2024.06.019
25. X. Y. Mao, H. Ding, L. Q. Chen, Internal resonance of a supercritically axially moving beam subjected to the pulsating speed, *Nonlinear Dyn.*, **95** (2019), 631–651. https://doi.org/10.1007/s11071-018-4587-1
26. A. Luongo, D. Zulli, Nonlinear energy sink to control elastic strings: the internal resonance case, *Nonlinear Dyn.*, **81** (2015), 425–435. https://doi.org/10.1007/s11071-015-2002-8
27. A. K. Abramian, W. T. van Horssen, S. A. Vakulenko, Oscillations of a string on an elastic foundation with space and time-varying rigidity, *Nonlinear Dyn.*, **88** (2017), 567–580. https://doi.org/10.1007/s11071-016-3261-8
28. N. H. Zhang, L. Q. Chen, Nonlinear dynamical analysis of axially moving viscoelastic strings, *Chaos Solitons Fractals*, **24** (2005), 1065–1074. https://doi.org/10.1016/j.chaos.2004.09.113
29. M. Babaz, L. Jezequel, C. H. Lamarque, P. Perrard, Unusual expression of tension of a massless cable with application to the oscillations of a mass suspended to a cable with a variable length, *J. Sound Vib.*, **363** (2016), 446–459. https://doi.org/10.1016/j.jsv.2015.10.020
30. Y. He, E. Chen, N. S. Ferguson, W. Zhu, Y. Lu, H. Wei, Solutions for the vibration of an axially moving variable length string system: Wave propagation versus space-time finite element predictions, *Mech. Syst. Signal Process.*, **210** (2024), 111090. https://doi.org/10.1016/j.ymssp.2023.111090
31. T. Guo, H. Kang, L. Wang, Y. Zhao, Cable's mode interactions under vertical support motions: Boundary resonant modulation, *Nonlinear Dyn.*, **84** (2016), 1259–1279. https://doi.org/10.1007/s11071-015-2565-4
32. T. Guo, H. Kang, L. Wang, Q. Liu, Y. Zhao, Modal resonant dynamics of cables with a flexible support: A modulated diffraction problem, *Mech. Syst. Signal Process.*, **106** (2018), 229–248. https://doi.org/10.1016/j.ymssp.2017.12.023
33. Y. D. Wang, Z. M. Chen, Three-Dimensional dynamic modelling and analysis of a Dual-Cable winding hoisting system, *Int. J. Struct. Stab. Dyn.*, **24** (2024), 2450178. https://doi.org/10.1142/S0219455424501785
34. Y. Zhao, C. Sun, Z. Wang, L. Wang, Analytical solutions for resonant response of suspended cables subjected to external excitation, *Nonlinear Dyn.*, **78** (2014), 1017–1032. https://doi.org/10.1007/s11071-014-1493-z

35. J. Wang, W. T. van Horssen, J. M. Wang, On resonances in transversally vibrating strings induced by an external force and a time-dependent coefficient in a robin boundary condition, *J. Sound Vib.*, **512** (2021), 116356. https://doi.org/10.1016/j.jsv.2021.116356
36. J. Zhang, J. Luo, Y. J. Pi, Wave response of the axially moving string with complex boundary conditions based on characteristic-line method and Duhamel's integral, *Nonlinear Dyn.*, **113** (2025), 16197–16223. https://doi.org/10.1007/s11071-025-10993-9
37. X. Arrasate, S. Kaczmarczyk, G. Almandoz, J. M. Abete, I. Isasa, The modelling, simulation and experimental testing of the dynamic responses of an elevator system, *Mech. Syst. Signal Process.*, **42** (2014), 258–282. https://doi.org/10.1016/j.ymssp.2013.05.021
38. N. V. Gaiko, W. T. van Horssen, Resonances and vibrations in an elevator cable system due to boundary sway, *J. Sound Vib.*, **424** (2018), 272–292. https://doi.org/10.1016/j.jsv.2017.11.054
39. S. H. Sandilo, W. T. van Horssen, On a cascade of autoresonances in an elevator cable system, *Nonlinear Dyn.*, **80** (2015), 1613–1630. https://doi.org/10.1007/s11071-015-1966-8
40. J. Wang, W. T. van Horssen, On resonances and transverse and longitudinal oscillations in a hoisting system due to boundary excitations, *Nonlinear Dyn.*, **111** (2023), 5079–5106. https://doi.org/10.1007/s11071-022-08052-8
41. J. Wang, W. T. van Horssen, Analysis of longitudinal oscillations in a vertically moving cable subject to nonclassical boundary conditions, *Appl. Math. Model.*, **111** (2022), 44–62. https://doi.org/10.1016/j.apm.2022.04.021
42. W. D. Zhu, L. J. Teppo, Design and analysis of a scaled model of a high-rise, high-speed elevator, *J. Sound Vib.*, **264** (2003), 707–731. https://doi.org/10.1016/S0022-460X(02)01218-X
43. Ministry of Emergency Management of the People's Republic of China, Coal Mine Safety Regulations of China (in Chinese), Emergency Management Press, Beijing, 2025. Available from: https://www.mem.gov.cn/gk/zfxxgkpt/fdzdgknr/202508/t20250804_553277.shtml.

Appendix

For clarity, subscripts u, w, and v denote the longitudinal, transverse, and lateral vibration components, respectively. Subscripts c and p denote the two cable segments considered in the model, and k = 1, 2 denotes the two suspension strings. The modal indices are denoted by i,j = 1, 2, …, n. Unless otherwise specified, each matrix block is an $n \times n$ matrix, whereas each generalized coordinate vector, nonlinear coupling vector, and generalized force vector is an $n \times 1$ vector.

A.1. Block definitions

The block matrices in Eq (4.9) are defined as follows:

$$\mathbf{M}_r = \operatorname{diag}\left(\mathbf{M}_{rc1}, \mathbf{M}_{rc2}, \mathbf{M}_{rp1}, \mathbf{M}_{rp2}\right), \quad r = u, w, v,$$

$$\mathbf{C}_r = \operatorname{diag}\left(\mathbf{C}_{rc1}, \mathbf{C}_{rc2}, \mathbf{C}_{rp1}, \mathbf{C}_{rp2}\right), \quad r = u, w, v,$$

$$\mathbf{K}_r = \operatorname{diag}\left(\mathbf{K}_{rc1}, \mathbf{K}_{rc2}, \mathbf{K}_{rp1}, \mathbf{K}_{rp2}\right), \quad r = u, w, v.$$

The corresponding generalized coordinate, nonlinear coupling, and generalized force vectors are as follows:

$$\mathbf{q}_r=\left(\mathbf{q}_{rc1}^{\mathrm{T}},\mathbf{q}_{rc2}^{\mathrm{T}},\mathbf{q}_{rp1}^{\mathrm{T}},\mathbf{q}_{rp2}^{\mathrm{T}}\right)^{\mathrm{T}},\quad r=u,w,v,$$

$$\mathbf{P}_r=\left(\mathbf{P}_{rc1}^{\mathrm{T}},\mathbf{P}_{rc2}^{\mathrm{T}},\mathbf{P}_{rp1}^{\mathrm{T}},\mathbf{P}_{rp2}^{\mathrm{T}}\right)^{\mathrm{T}},\quad r=u,w,v,$$

$$\mathbf{F}_r=\left(\mathbf{F}_{rc1}^{\mathrm{T}},\mathbf{F}_{rc2}^{\mathrm{T}},\mathbf{F}_{rp1}^{\mathrm{T}},\mathbf{F}_{rp2}^{\mathrm{T}}\right)^{\mathrm{T}},\quad r=u,w,v.$$

A.2. Mass matrix entries

$$M_{uck,ij}=\rho+\frac{I_d}{l_{ck}R_d^2}\phi_{ck}^i(0)\phi_{ck}^j(0)+\frac{I_h}{l_{ck}R_h^2}\phi_{ck}^i(1)\phi_{ck}^j(1),$$

$$M_{wck,ij}=M_{vck,ij}=\rho,$$

$$M_{upk,ij}=\rho+\frac{I_h}{l_{pk}R_h^2}\phi_{pk}^i(0)\phi_{pk}^j(0)+\frac{m_k+\mu_e k_p S_k}{l_{pk}}\phi_{pk,i}(1)\phi_{pk,j}(1),$$

$$M_{wpk,ij}=M_{vpk,ij}=\rho.$$

A.3. Damping matrix entries

$$C_{uck,ij}=\frac{2\rho V}{l_{ck}}\int_0^1\phi'_{ck,i}\phi_{ck,j}\mathrm{d}\psi-\frac{c_h}{l_{ck}}\phi_{ck,i}(1)\phi_{ck,j}(1),$$

$$C_{wck,ij}=\frac{2\rho V}{l_{ck}}\int_0^1\varphi'_{ck,i}\varphi_{ck,j}\mathrm{d}\psi,$$

$$C_{vck,ij}=\frac{2\rho V}{l_{ck}}\int_0^1\xi'_{ck,i}\xi_{ck,j}\mathrm{d}\psi,$$

$$C_{upk,ij}=\frac{2\rho V}{l_{pk}}\int_0^1\left(1-\psi_{pk}\right)\phi'_{pk,i}\phi_{pk,j}\mathrm{d}\psi,$$

$$C_{wpk,ij}=\frac{2\rho V}{l_{pk}}\int_0^1\left(1-\psi_{pk}\right)\varphi'_{pk,i}\varphi_{pk,j}\mathrm{d}\psi+\frac{c_d}{l_{pk}}\varphi_{pk,i}(1)\varphi_{pk,j}(1),$$

$$C_{vpk,ij}=\frac{2\rho V}{l_{pk}}\int_0^1\left(1-\psi_{pk}\right)\xi'_{pk,i}\xi_{pk,j}\mathrm{d}\psi+\frac{c_d}{l_{pk}}\xi_{pk,i}(1)\xi_{pk,j}(1).$$

A.4. Stiffness matrix entries

$$K_{uck,ij}=\frac{\rho a}{l_{ck}}\int_0^1\phi'_{ck,i}\phi_{ck,j}\mathrm{d}\psi+\frac{\rho V^2}{l_{ck}^2}\int_0^1\phi''_{ck,i}\phi_{ck,j}\mathrm{d}\psi-\frac{EA}{l_{ck}^2}\int_0^1\phi''_{ck,i}\phi_{ck,j}\mathrm{d}\psi,$$

$$
\begin{aligned}
K_{wck,ij} &= \frac{\rho a-\rho g\sin\alpha}{l_{ck}}\int_0^1 \varphi'_{ck,i}\varphi_{ck,j}\mathrm{d}\psi+\frac{\rho V^2}{l_{ck}^2}\int_0^1 \varphi''_{ck,i}\varphi_{ck,j}\mathrm{d}\psi \\
&+\frac{\rho g\sin\alpha}{l_{ck}}\int_0^1 \varphi''_{ck,i}\varphi_{ck,j}\mathrm{d}\psi-\frac{\left(m_k+\rho l_{vk}+\mu_e k_p S_k\right)g}{l_{ck}^2}\int_0^1 \varphi''_{ck,i}\varphi_{ck,j}\mathrm{d}\psi,
\end{aligned}
$$

$$
\begin{aligned}
K_{vck,ij} &= \frac{\rho a-\rho g\sin\alpha}{l_{ck}}\int_0^1 \xi'_{ck,i}\xi_{ck,j}\mathrm{d}\psi+\frac{\rho V^2}{l_{ck}^2}\int_0^1 \xi''_{ck,i}\xi_{ck,j}\mathrm{d}\psi \\
&+\frac{\rho g\sin\alpha}{l_{ck}}\int_0^1 \xi''_{ck,i}\xi_{ck,j}\mathrm{d}\psi-\frac{\left(m_k+\rho l_{vk}+\mu_e k_p S_k\right)g}{l_{ck}^2}\int_0^1 \xi''_{ck,i}\xi_{ck,j}\mathrm{d}\psi,
\end{aligned}
$$

$$
K_{upk,ij}=\frac{\rho a}{l_{pk}}\int_0^1\left(1-\psi_{pk}\right)\phi'_{pk,i}\phi_{pk,j}\mathrm{d}\psi+\frac{\rho V^2}{l_{pk}^2}\int_0^1\left(1-\psi_{pk}\right)^2\phi''_{pk,i}\phi_{pk,j}\mathrm{d}\psi-\frac{EA}{l_{pk}^2}\int_0^1\phi''_{pk,i}\phi_{pk,j}\mathrm{d}\psi \text{ ,}
$$

$$
\begin{aligned}
K_{wpk,ij} &= \frac{\rho a}{l_{pk}}\int_0^1\left(1-\psi_{pk}\right)\varphi'_{pk,i}\varphi_{pk,j}\mathrm{d}\psi+\frac{\rho V^2}{l_{pk}^2}\int_0^1\left(1-\psi_{pk}\right)^2\varphi''_{pk,i}\varphi_{pk,j}\mathrm{d}\psi \\
&-\frac{\rho g}{l_{pk}}\int_0^1\left(1-\psi_{pk}\right)\varphi''_{pk,i}\varphi_{pk,j}\mathrm{d}\psi-\frac{\left(m_k+\mu_e k_p S_k\right)g}{l_{pk}^2}\int_0^1\varphi''_{pk,i}\varphi_{pk,j}\mathrm{d}\psi \text{ ,} \\
&+\frac{k_p}{l_{pk}}\varphi_{pk,i}(1)\varphi_{pk,j}(1)
\end{aligned}
$$

$$
\begin{aligned}
K_{vpk,ij} &= \frac{\rho a}{l_{pk}}\int_0^1\left(1-\psi_{pk}\right)\xi'_{pk,i}\xi_{pk,j}\mathrm{d}\psi+\frac{\rho V^2}{l_{pk}^2}\int_0^1\left(1-\psi_{pk}\right)^2\xi''_{pk,i}\xi_{pk,j}\mathrm{d}\psi \\
&-\frac{\rho g}{l_{pk}}\int_0^1\left(1-\psi_{pk}\right)\xi''_{pk,i}\xi_{pk,j}\mathrm{d}\psi-\frac{\left(m_k+\mu_e k_p S_k\right)g}{l_{pk}^2}\int_0^1\xi''_{pk,i}\xi_{pk,j}\mathrm{d}\psi \text{ .} \\
&+\frac{k_p}{l_{pk}}\xi_{pk,i}(1)\xi_{pk,j}(1)
\end{aligned}
$$

A.5. Nonlinear coupling vector entries

$$
\begin{aligned}
P_{uck,j} &= -\frac{EA}{l_{ck}^3}\int_0^1\left(\sum_{i=1}^n\varphi'_{ck,i}q_{uck,i}\right)\left(\sum_{i=1}^n\varphi''_{ck,i}q_{wck,i}\right)\phi_{ck,j}\mathrm{d}\psi \\
&-\frac{EA}{l_{ck}^3}\int_0^1\left(\sum_{i=1}^n\xi'_{ck,i}q_{uck,i}\right)\left(\sum_{i=1}^n\xi''_{ck,i}q_{vck,i}\right)\phi_{ck,j}\mathrm{d}\psi
\end{aligned}
\text{ ,}
$$

$$
\begin{aligned}
P_{wck,j} &= -\frac{EA}{l_{ck}^3}\int_0^1\left(\sum_{i=1}^n\phi'_{ck,i}q_{uck,i}\right)\left(\sum_{i=1}^n\varphi''_{ck,i}q_{wck,i}\right)\varphi_{ck,j}\mathrm{d}\psi \\
&-\frac{EA}{l_{ck}^3}\int_0^1\left(\sum_{i=1}^n\phi''_{ck,i}q_{uck,i}\right)\left(\sum_{i=1}^n\varphi'_{ck,i}q_{wck,i}\right)\varphi_{ck,j}\mathrm{d}\psi \\
&-\frac{EA}{l_{ck}^3}\int_0^1\left(\sum_{i=1}^n\xi'_{ck,i}q_{vck,i}\right)\left(\sum_{i=1}^n\xi''_{ck,i}q_{vck,i}\right)\left(\sum_{i=1}^n\varphi'_{ck,i}q_{wck,i}\right)\varphi_{ck,j}\mathrm{d}\psi \\
&-\frac{3EA}{2l_{ck}^4}\int_0^1\left(\sum_{i=1}^n\varphi'_{ck,i}q_{wck,i}\right)^2\left(\sum_{i=1}^n\varphi''_{ck,i}q_{wck,i}\right)\varphi_{ck,j}\mathrm{d}\psi \\
&-\frac{EA}{l_{ck}^4}\int_0^1\left(\sum_{i=1}^n\xi'_{ck,i}q_{vck,i}\right)^2\left(\sum_{i=1}^n\varphi''_{ck,i}q_{wck,i}\right)\varphi_{ck,j}\mathrm{d}\psi
\end{aligned}
\text{ ,}
$$

$$
\begin{aligned}
P_{vck,j} = & -\frac{EA}{l_{ck}^3}\int_0^1\left(\sum_{i=1}^{n}\phi'_{ck,i}q_{uck,i}\right)\left(\sum_{i=1}^{n}\xi''_{ck,i}q_{vck,i}\right)\xi_{ck,j}\,\mathrm{d}\psi \\
& -\frac{EA}{l_{ck}^3}\int_0^1\left(\sum_{i=1}^{n}\phi''_{ck,i}q_{uck,i}\right)\left(\sum_{i=1}^{n}\xi'_{ck,i}q_{vck,i}\right)\xi_{ck,j}\,\mathrm{d}\psi \\
& -\frac{EA}{l_{ck}^3}\int_0^1\left(\sum_{i=1}^{n}\varphi'_{ck,i}q_{wck,i}\right)\left(\sum_{i=1}^{n}\varphi''_{ck,i}q_{wck,i}\right)\left(\sum_{i=1}^{n}\xi'_{ck,i}q_{vck,i}\right)\xi_{ck,j}\,\mathrm{d}\psi \\
& -\frac{3EA}{2l_{ck}^4}\int_0^1\left(\sum_{i=1}^{n}\xi'_{ck,i}q_{vck,i}\right)^2\left(\sum_{i=1}^{n}\xi''_{ck,i}q_{vck,i}\right)\xi_{ck,j}\,\mathrm{d}\psi \\
& -\frac{EA}{l_{ck}^4}\int_0^1\left(\sum_{i=1}^{n}\varphi'_{ck,i}q_{wck,i}\right)^2\left(\sum_{i=1}^{n}\xi''_{ck,i}q_{vck,i}\right)\xi_{ck,j}\,\mathrm{d}\psi
\end{aligned},
$$

$$
\begin{aligned}
P_{upk,j} = & -\frac{EA}{l_{pk}^3}\int_0^1\left(\sum_{i=1}^{n}\varphi'_{pk,i}q_{upk,i}\right)\left(\sum_{i=1}^{n}\varphi''_{pk,i}q_{wpk,i}\right)\phi_{pk,j}\,\mathrm{d}\psi \\
& -\frac{EA}{l_{pk}^3}\int_0^1\left(\sum_{i=1}^{n}\xi'_{pk,i}q_{upk,i}\right)\left(\sum_{i=1}^{n}\xi''_{pk,i}q_{vpk,i}\right)\phi_{pk,j}\,\mathrm{d}\psi
\end{aligned},
$$

$$
\begin{aligned}
P_{wpk,j} = & -\frac{EA}{l_{pk}^3}\int_0^1\left(\sum_{i=1}^{n}\phi'_{pk,i}q_{upk,i}\right)\left(\sum_{i=1}^{n}\varphi''_{pk,i}q_{wpk,i}\right)\varphi_{pk,j}\,\mathrm{d}\psi \\
& -\frac{EA}{l_{pk}^3}\int_0^1\left(\sum_{i=1}^{n}\phi''_{pk,i}q_{upk,i}\right)\left(\sum_{i=1}^{n}\varphi'_{pk,i}q_{wpk,i}\right)\varphi_{pk,j}\,\mathrm{d}\psi \\
& -\frac{3EA}{2l_{pk}^4}\int_0^1\left(\sum_{i=1}^{n}\varphi'_{pk,i}q_{wpk,i}\right)^2\left(\sum_{i=1}^{n}\varphi''_{pk,i}q_{wpk,i}\right)\varphi_{pk,j}\,\mathrm{d}\psi \\
& -\frac{EA}{l_{pk}^3}\int_0^1\left(\sum_{i=1}^{n}\xi'_{pk,i}q_{vpk,i}\right)\left(\sum_{i=1}^{n}\xi''_{pk,i}q_{vpk,i}\right)\left(\sum_{i=1}^{n}\varphi'_{pk,i}q_{wpk,i}\right)\varphi_{pk,j}\,\mathrm{d}\psi \\
& -\frac{EA}{l_{pk}^4}\int_0^1\left(\sum_{i=1}^{n}\xi'_{pk,i}q_{vpk,i}\right)^2\left(\sum_{i=1}^{n}\varphi''_{pk,i}q_{wpk,i}\right)\varphi_{pk,j}\,\mathrm{d}\psi
\end{aligned},
$$

$$
\begin{aligned}
P_{vpk,j} = & -\frac{EA}{l_{pk}^3}\int_0^1\left(\sum_{i=1}^{n}\phi'_{pk,i}q_{upk,i}\right)\left(\sum_{i=1}^{n}\xi''_{pk,i}q_{vpk,i}\right)\xi_{pk,j}\,\mathrm{d}\psi \\
& -\frac{EA}{l_{pk}^3}\int_0^1\left(\sum_{i=1}^{n}\phi''_{pk,i}q_{upk,i}\right)\left(\sum_{i=1}^{n}\xi'_{pk,i}q_{vpk,i}\right)\xi_{pk,j}\,\mathrm{d}\psi \\
& -\frac{3EA}{2l_{pk}^4}\int_0^1\left(\sum_{i=1}^{n}\xi'_{pk,i}q_{vpk,i}\right)^2\left(\sum_{i=1}^{n}\xi''_{pk,i}q_{vpk,i}\right)\xi_{pk,j}\,\mathrm{d}\psi \\
& -\frac{EA}{l_{pk}^3}\int_0^1\left(\sum_{i=1}^{n}\varphi'_{pk,i}q_{wpk,i}\right)\left(\sum_{i=1}^{n}\varphi''_{pk,i}q_{wpk,i}\right)\left(\sum_{i=1}^{n}\xi'_{pk,i}q_{vpk,i}\right)\xi_{pk,j}\,\mathrm{d}\psi \\
& -\frac{EA}{l_{pk}^4}\int_0^1\left(\sum_{i=1}^{n}\varphi'_{pk,i}q_{wpk,i}\right)^2\left(\sum_{i=1}^{n}\xi''_{pk,i}q_{vpk,i}\right)\xi_{pk,j}\,\mathrm{d}\psi
\end{aligned}.
$$

A.6. Generalized force vector entries

$$
F_{uck,j} = \rho\left(a - g\sin\alpha\right)\int_0^1 \phi_{ck,j}\,\mathrm{d}\psi + \frac{I_d}{l_{ck}R_d^2}a\phi_{ck}^j\left(0\right) + \frac{I_h}{l_{ck}R_h^2}a\phi_{ck,j}\left(1\right),
$$

$$
F_{wck,j} = F_{vck,j} = F_{vpk,j} = 0,
$$

$$
F_{upk,j} = \rho a\int_0^1 \phi_{pk,j}\,\mathrm{d}\psi + \frac{I_h}{l_{pk}R_h^2}a\phi_{pk}^j\left(0\right) + \frac{\left(m_k + \mu_e k_p S_k\right)a}{2l_{pk}}\phi_{pk,j}\left(1\right),
$$

$$F_{wpk,j} = \frac{k_{pk}}{l_{pk}} S_k \varphi_{pk,j}(1) + \frac{c_{dk}}{l_{pk}} \dot{S}_k \varphi_{pk,j}(1).$$

A.7. Generalized coordinate vectors

The generalized coordinate vectors can be written compactly as

$$\mathbf{q}_{rks} = \left[q_{rsk,1}(t) \quad q_{rsk,2}(t) \quad \cdots \quad q_{rsk,n}(t) \right]^{\mathrm{T}}, \quad r = u, w, v, \quad s = c, p, \quad k = 1, 2.$$

AIMS Press

©2026 the Author(s), licensee AIMS Press. This is an open access article distributed under the terms of the Creative Commons Attribution License (https://creativecommons.org/licenses/by/4.0)